IRAQI JOURNAL OF APPLIED PHYSICS

The *Iraqi Journal of Applied Physics (IJAP)* is a peer reviewed journal of high quality devoted to the publication of original research papers from applied physics and their broad range of applications. IJAP publishes quality original research papers, comprehensive review articles, survey articles, book reviews, dissertation abstracts in physics and its applications in the broadest sense. It is intended that the journal may act as an interdisciplinary forum for Physics and its applications. Innovative applications and material that brings together diverse areas of Physics are particularly welcome. Review articles in selected areas are published from time to time. It aims to disseminate knowledge; provide a learned reference in the field; and establish channels of communication between academic and research experts, policy makers and executives in industry, commerce and investment institutions. IJAP is a quarterly specialized periodical dedicated to publishing original papers, letters and reviews in: Applied & Nonlinear Optics, Applied Mechanics & Thermodynamics, Digital & Optical Communications, Electronic Materials & Devices, Laser Physics & Applications, Plasma Physics & Applications, Quantum Physics & Spectroscopy, Semiconductors & Optoelectronics, and Solid State Physics & Applications

SPONSORED AND PUBLISHED BY
THE IRAQI SOCIETY FOR ALTERNATIVE AND RENEWABLE ENERGY SOURCES & TECHNIQUES (I.S.A.R.E.S.T.)

ISSN 1813-2065

IRAQI JOURNAL OF APPLIED PHYSICS

" INSTRUCTIONS TO AUTHORS "

CONTRIBUTIONS

Contributions to be published in this journal should be original research works, i.e., those not already published or submitted for publication elsewhere, individual papers or letters to editor.

SUBMISSION OF MANUSCRIPTS

Manuscripts should be submitted to the editor at the mailing address:

Iraqi Journal of Applied Physics
Editorial Board
P. O. Box 55259, Baghdad 12001, IRAQ
submission@ijap.org , editor@ijap.org

MANUSCRIPTS

Two hard copies with soft copy on a compact disc (CD) should be submitted to Editor in the following configuration:

- Double-spaced one-side A4 size with 2.5 cm margins of all sides
- Times New Roman font (16pt bold for title, 14pt bold for names, 12pt bold for headings, 12pt regular for text)
- Letters should not exceed 10 pages, papers should not exceed 20 pages and reviews are up to author.
- Manuscripts presented in English only are accepted.
- English abstract not exceed 150 words
- 4 keywords (at least) should be maintained on (PACS preferred)
- Author(s) should express all quantities in SI units
- Equations should be written in equation form (*italic* and symbolic)
- Figures and Tables should be separated from text
- Figures and diagrams can be submitted in colors for assessment and they will be returned to authors after provide printable copies
- Charts should be indicated by the software used for
- Only original or high-resolution scanner photos are accepted
- For electronic submission, articles should be formatted with MS-Word software.

AUTHOR NAMES AND AFFILIATIONS

It is IJAP policy that all those who have participated significantly in the technical aspects of a paper be recognized as co-authors or cited in the acknowledgments. In the case of a paper with more than one author, correspondence concerning the paper will be sent to the first author unless staff is advised otherwise.

Author name should consist of first name, middle initial, last name. The author affiliation should consist of the following, as applicable, in the order noted:

- Company or college (with department name or company division)
- Postal address
- City, state, zip code
- Country name
- Telephone, and e-mail

REFERENCES

The references should be brought at the end of the article, and numbered in the order of their appearance in the paper. The reference list should be cited in accordance with the following examples:

[1] X. Ning and M.R. Lovell, "On the Sliding Friction Characteristics of Unidirectional Continuous FRP Composites", *ASME J. Tribol.*, 124(1) (2002) 5-13.

[2] M. Barnes, "Stresses in Solenoids", *J. Appl. Phys.*, 48(5) (2001) 2000–2008.

[3] J. Jones, "Contact Mechanics", Cambridge University Press (Cambridge, UK) (2000), Ch.6, p.56.

[4] Y. Lee, S.A. Korpela and R. Horne, "Structure of Multi-Cellular Natural Convection in a Tall Vertical Annulus", Proc. 7th International Heat Transfer Conference, U. Grigul et al., eds., Hemisphere (Washington DC), 2 (1982) 221–226.

[5] M. Hashish, "Waterjet Technology Development", High Pressure Technology, PVP-Vol. 406 (2000), 135-140.

[6] D.W. Watson, "Thermodynamic Analysis", ASME Paper No. 97-GT-288 (1997).

[7] C.Y. Tung, "Evaporative Heat Transfer in the Contact Line of a Mixture", Ph.D. thesis, Rensselaer Polytechnic Institute, Troy, NY (1982).

PROOFS

Authors will receive proofs of papers and are requested to return one corrected hard copy with a WORD copy on a compact disc (CD). New materials inserted in the original text without Editor permission may cause rejection of paper.

COPYRIGHT FORM

Author(s) will be asked to transfer copyrights of the article to the Journal soon after acceptance of it. This will ensure the widest possible dissemination of information.

OFFPRINTS

Authors will receive offprints free of charge and any additional offprints can be ordered.

SUBSCRIPTION AND ORDERS

Annual fees (4 issues per year) of subscription are:

- 50 US$ for individuals inside Iraq.
- 100 US$ for establishments inside Iraq.
- 100 US$ for individuals abroad.
- 200 US$ for establishments abroad.

Fees are reduced by 25% for I.S.A.R.E.S.T. members. Orders of issues can be submitted by contacting the editor-in-chief or editorial office at **subscription@ijap.org** to maintain the address of issue delivery and payment way.

Da-Tren Chou

Key Principle of Electroluminescent Polymers (Review Article)

Department of Biomedical Engineering, Case Western Reserve University, Cleveland, USA

Recent progress made in the field of electroluminescent (EL) polymers is reviewed in this paper. Polymer electroluminescence is an area of growing interest due to its appeal in a scientific sense and for its potential in applications for low-cost, easily constructible light emitting diodes (LEDs) and in large flat displays. A brief overview of device construction is presented followed by a review of new developments in methods for fabrication and synthesis of EL polymer devices. Characteristics of EL polymer devices are considered with the mechanisms used to generate them.

Keywords: Electroluminescent, Polymers, LED, Microfabrication
Received: 3 February 2009, **Accepted**: 10 February 2009

1. Introduction

Electroluminescent (EL) polymers are organic polymers that emit light upon the incidence of an electric field. The first discovery of electroluminescence for inorganic compounds was by Destriau in 1936 [1]. In 1947, it was found that a transparent anode of a layer of Indium Tin Oxide (ITO) deposited on glass could be used to allow for light emitting devices on a planar surface. The first observation of electroluminescence in organic crystals was made in 1963 for crystals of antracene using silver paste electrodes and several hundred volts for emission to take place [2]. The characteristics of devices using such technology were considerably worse than those of inorganic devices which consequently received greater focus. Interest in the electroluminescent polymers was revitalized when major works from Tang and van Slyke [3] and Saito and Tsutsui et al. [4] were published in the late 1980s which concerned new light-emitting diodes (LEDs) with organic fluorescent dyes. Advances in semiconducting polymers aided the construction of organic LEDs with much research being focused on poly(*p*-phenylene-vinylene) (PPV) as the active material.

Polymer LEDs in their basic form consist of the electroluminescent polymer film, a transparent anode (most often ITO coated glass substrate), a metallic cathode, and a power source which can be either AC or DC. The cathode is an electropositive low work function metal such as calcium, magnesium, or aluminum and is evaporated onto the polymer in vacuo. The EL polymer may be deposited on the anode by spin or dip-coating to a thickness of about 100nm. When an external voltage is applied at the electrodes, charge carriers called 'holes' at the anode, and electrons at the cathode, are injected into the polymer film past the threshold voltage for the active material. After imposition of an electric field, the charge carriers move through the active film and are discharged without radiation when they arrive at the electrode. But if a hole and an electron meet while traveling through the polymer material, singlet and triplet states are excited and excitons are formed. Radiation occurs to relax the singlet state and light passes through the transparent anode.

The purpose of this review paper is to examine recent advances in electroluminescent polymers in LEDs, specifically methods for their construction as well as their features and potential applications.

2. Microfabrication of diode pixel arrays

The fabrication of microscopic LEDs to create pixel arrays of organic LEDs is an important concept in the development of flat panel electroluminescent displays. Using photoablation, a micron sized pixilated array or polymer was created [5]. The polymer used in the microfabrication was a conjugated copolymer of benzene and pyridine units – copoly-(1,4-phenylenevinylene-2,6 pyridylenevinylene) or co(*PV-PyV*). An increased DC voltage led to a shift from the green-yellow region to the red for the main emission band, demonstrating that the emission properties could be adjusted and that superimposing AC voltage on small biased DC

 ISSN 1813-2065

voltage enhances EL emission by multiple magnitudes, yielding an EL spectrum similar to that of PPV.

The setup of the array utilized an electron microscope bar grid on a layer of ITO coated on a glass substrate. An excimer laser between the thresholds of the ITO ablation and glass substrate was used to replicate the dimensions of the grid onto the ITO anode. Layers of the polymer were baked and spin coated on the ITO and laser ablation was performed for the cathode layer and partly for the polymer layer over the bar grid. Light intensity had significant improvements over past investigations of thin film LEDs with the same electrodes under the same conditions. The electroluminescence from the pixel array was improved likely because of enhanced electric fields at the pixels. Using voltage tuning to adjust emission properties, multicolor displays of high resolution are a definite possibility.

3. Patterned light emission

Several methods for creating patterned light emission have been investigated. One such technique is microcontact printing. In a recent method [6], a patterned elastomer (PDMS) was first molded with a relief structure. The self-assembling monolayer (SAM) was formed by conformal contact between the inked PDMS stamp and the ITO. The PPV was selectively deposited on hydrophilic regions of the SAM. A clear topographical contrast-pattern was observed in this process of relative simplicity and low cost.

Rogers et al. [7] developed a system for microfabrication of patterned polymer LEDs through solvent assisted micromolding. An elastomeric mold was formed from casting and curing a prepolymer against a relief structure. This was used to generate a PPV precursor film with the surface relief of the mold. The process demonstrated a way to use patterned layers to spatially modify the intensity of the emitted light. It was achieved using the most basic materials for single layer polymer LEDs, but can be applied for electron-transporting, hole-transporting, or insulating layers.

4. Multi-color organic EL devices

Fabrication of patterned light-emitting layers is important for the creation of multi-color devices. Following are specific techniques in constructing multi-color devices. In an effort to create a red, green, and blue (RGB) polymer OLED, soluble polymers with oxetane sidegroups crosslinked photochemically to form insoluble polymer networks with photoresist properties were used [8]. A recent procedure [9] was used to synthesize the RGB light emitting oxetane-functionalized spirobiflourene-*co*-flourene polymers. The three polymers were used in OLED devices and were shown to crosslink without major changes to their EL properties. To photo-pattern the films, the layers were irradiated through a shadow mask and immersed in tetrahydrofuran. The efficiencies of the EL polymers did not reach their optimal levels except for the blue-emitting material. This shortcoming may be remedied through better synthesis.

Significant attention has been given to the development of full panel displays using pixel arrays for RGB emission. A pyramid pixel structure has been developed [10] which integrated the OLEDs in full color emission by placing the RBG LEDs on the walls of the pyramid, emitting light through the base of the pyramid. This allows the LEDs to share the same area to form a color. This structure allows for a high resolution and full color, without using the shadow mask.

5. Self-assembled films

Construction of multilayer organic LEDs may also be conducted through deposition of layer-by-layer self-assembled films. Layer-by-layer self-assembly methods rely on electrostatic interaction of anion and cation pairs in successive absorption steps. Recent advances have allowed for the fabrication of thin film multilayer heterostructures with unparalleled control over type and thickness of the layers [11]. PPV precursor polymer was fabricated into thin self-assembled films by alternating layers of a polycation (PPV) and polyanion. This process shows potential to make large area uniform thin films. However, the multilayer and monolayer LED showed a shift in their respective spectra.

A recent experiment [12] compared methods for layer-by-layer self-assembled film deposition in which a different electrostatic adsorption process was shown to have advantages over the conventional method. In the experient, an organic dye, alizarin violet, when acting as an anion, tended to leave the films during later polycation deposition, causing lower intensities of the absorption band maxima of alizarin. An alternative approach did not show evidence of material loss during polyction deposition, and was conducted by electrostatically anchoring the alizarin molecules to the polycation before deposition. The simplicity of this model for layer-by-layer self-assembled films suggests that the technique can be applied to other dye molecules using few charged groups with a polyanion and polycation while avoiding material losses.

6. Polarized electroluminescence

The state of polarization of emitted light may be controlled by using liquid crystalline polymers [13]. Besides the anisotropic characteristic, liquid crystalline polymers in LEDs also yielded spontaneously homogenous monodomain films. Linear or elliptical polarized emission was obtained due to the inherent structure of the liquid crystalline polymer and its optical properties, which may be used to control the polarization. Further research should lead to higher macroscopical orientations. An issue concerning elliptical polarized emission is that a high degree of ellipticity requires larger than idea film thicknesses.

7. Surface light emitting devices

An interesting alternative to the conventional setup of an EL polymer between a transparent anode and a cathode is the surface light emitting device (SLED) where both the anode and cathode are underneath the polymer, rendering transparency of the anode unnecessary. A recent study used EO-PT, a conjugated polymer based on polythiophene with oligo(ethyleneoxide) side chains as the EL polymer [14]. The two methods of constructing the SLED are vertical (V-SLED) and lateral (L-SLED) and are shown in Fig. (1) [14].

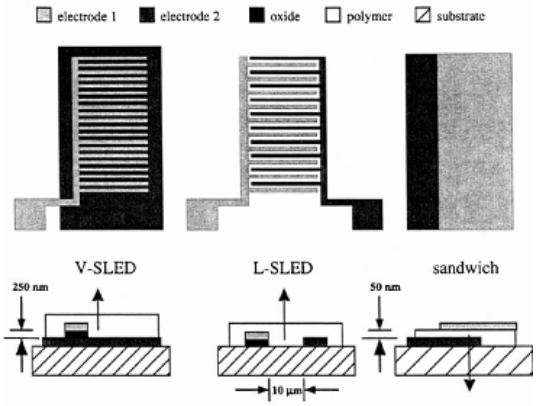

Fig. (1) V-SLED, L-SLED, and sandwich electrode configuration with electrode separations and and arrows for the direction of light emitted

The closer the electrode spacing, the greater the current transmitted and hense more light was emitted. SLEDs constructed with ITO and aluminum had lower turn-on voltages and greater currents than those with gold-silicide and aluminum electrodes as well as better stability. The addition of salt to the polymer resulted in an increase in the current and brightness, a decrease in turn-on voltage, and the current-voltage characteristics to be symmetric.

Microfabrication of surface light-emitting diodes on silicon substrates [15] was totally compatible with with conventional silicon processing. This was because the polymer was spin coated last and the light was emitted from the top of the diode. The voltages needed for light emission were still not much greater than those of the standard sandwich LEDs.

8. Conclusions

The potential for the numerous recent developments in electroluminescent polymers in LEDs is quite promising. With continued attention, the techniques described here could lead to a number of fruitful uses. As techniques for organic LEDs progress, greater control over characteristics such as polarization, emission intensity, and resolution will emerge, as well various applications – namely inexpensive large-area multicolor displays.

References

[1] G. Destriau, *J. Chem. Phys*., 33 (1936) 587–625.
[2] M. Pope, H.P. Kallmann and P. Magnante, *J. Chem. Phys*., 38(8) (1963) 2042.
[3] C.W. Tang and S.A. van Slyke, *Appl. Phys. Lett.*, 51(12) (1987) 913–9155.
[4] C. Adachi, T. Tsutsui and S. Saito, *Appl. Phys. Lett*., 56(9) (1990) 799–801. Also, C. Adachi et al., *Jpn. J. Appl. Phys.*, 27(2) (1998) L269–271.
[5] E.Z. Faraggi et al., *Synth. Met*., 85(1-3) (1997) 1187–1190.
[6] M.J. Park et al., *J. Nonlinear Opt. Phys. Mat*., 13 (2004) 643-647.
[7] J.A. Rogers, Z. Bao and L. Dhar, *Appl. Phys. Lett*., 73(3) (1998) 294–296.
[8] D.C. Muller et al., *Nature*, 421 (2003) 829-833.
[9] H. Becker et al., *SID Digest Tech. Pap*., 33 (2002) 780–782.
[10] Y. Yang and S. Chang, *Appl. Phys. Lett*., 77(7) (2000) 936-938.
[11] M. Onoda and K. Yoshino, *J. Appl. Phys*., 78(7) (1995) 4456–4462.
[12] S. Das and A.J. Pal, *Langmuir*, 18 (2002) 458–461.
[13] K.U.W. Clauswitz ey al., *Synth. Met.*, 111-112 (2000) 169–71.
[14] Y. Kaminorz et al., *Synth. Met*., 113(1-2) (2000) 103–114.
[15] E. Smela et al., *Semicond. Sci. Technol*., 13 (1998) 433–439.

The Third International Conference on Advanced Engineering Computing and Applications in Sciences

ADVCOMP 2009

October 11-16, 2009 - Sliema, Malta

Call for Papers

With the advent of high performance computing environments, virtualization, distributed and parallel computing, as well as the increasing memory, storage and computational power, processing particularly complex scientific applications and voluminous data is more affordable. With the current computing software, hardware and distributed platforms effective use of advanced computing techniques is more achievable.

The goal of the International Conference on Advanced Engineering Computing and Applications in Sciences, ADVCOMP 2009, is to bring together researchers from the academia and practitioners from the industry in order to address fundamentals of advanced scientific computing and specific mechanisms and algorithms for particular sciences. The conference will provide a forum where researchers shall be able to present recent research results and new research problems and directions related to them. The conference seeks contributions presenting novel research in all aspects of new scientific methods for computing and hybrid methods for computing optimization, as well as advanced algorithms and computational procedures, software and hardware solutions dealing with specific domains of science.

The topics suggested by the conference can be discussed in term of concepts, state of the art, research, standards, implementations, running experiments, applications, and industrial case studies. Authors are invited to submit complete unpublished papers, which are not under review in any other conference or journal in the following, but not limited to, topic areas. All tracks are open to both research and industry contributions.

Advances on computing theories

Finite-state machines, Petri nets/stochastic/colored/probabilistic/etc
Genetic algorithms, Machine learning theory, Prediction theory, Bayesian theory, /statistics/filtering/estimation/reasoning/rating/etc
Markov chains/process/model/etc
Graphs theories

Advances in computation methods

Hybrid computational methods, Advanced numerical algorithms, Differential calculus, Matrix perturbation theory, Rare matrices, Fractals & super-fractal algorithms, Random graph dynamics, Multi-dimensional harmonic estimation

Computational logics

Knowledge-based systems and automated reasoning Logical issues in knowledge representation /non-monotonic reasoning/belief, Specification and verification of programs and systems, Applications of logic in hardware and VLSI, Natural language, concurrent computation, planning
Deduction and reasoning, Logic of computation, Dempster-Shafer theory, Fuzzy theory/computation/logic/etc

Advances on computing mechanisms

Clustering large and high dimensional data, Data fusion and aggregation, Biological sequence analysis, Biomecatronics mechanisms, Biologically inspired mechanisms, System theory and control mechanisms, Multi-objective evolutionary algorithms, Constraint-based algorithms, Ontology-based reasoning, Topology and structure patterns, Geometrical pattern similarity, Strong and weak symmetry, Distortion in coordination mechanisms

Computing techniques

Distributed computing, Parallel computing, Grid computing, Autonomic computing, Cloud computing, Development of numerical and scientific software-based systems, Pattern-based computing, Finite-element method computation, Elastic models, Optimization techniques, Simulation techniques, Stream-based computing

Development of computing support

Computing platforms, Advanced scientific computing, Support for scientific problem-solving, Support for distributed decisions, Agent-assisted workflow support, Middleware computation support, High performance computing, Problem solving environments, Computational science and education, Neuronal networks

Cloud computing

Hardware-as-a-service, Software-as-a-service [SaaS applicaitions], Platform-as-service, On-demand computing models, Cloud Computing programming and application development, Scalability, discovery of services and data in Cloud computing infrastructures, Privacy, security, ownership and reliability issues, Performance and QoS, Dynamic resource provisioning, Power-efficiency and Cloud computing Load balancing, Application streaming, Cloud SLAs, business models and pricing policies, Custom platforms, Large-scale compute infrastructures, Managing applications in the clouds, Data centers, Process in the clouds, Content and service distribution in Cloud computing infrastructures, Multiple applications can run on one computer (virtualization a la VMWare), Grid computing (multiple computers can be used to run one application), Cloud-computing vendor governance and regulatory compliance

Grid Networks, Services and Applications

GRID theory, frameworks, methodologies, architecture, ontology, GRID infrastructure and technologies, GRID middleware, GRID protocols and networking, GRID computing, utility computing, autonomic computing, metacomputing, Programmable GRID, Data GRID, Context ontology and management in GRIDs, Distributed decisions in GRID networks, GRID services and applications, Virtualization, modeling, and metadata in GRID, Resource management, scheduling, and scalability in GRID, GRID monitoring, control, and management, Traffic and load balancing in GRID, User profiles and priorities in GRID, Performance and security in GRID systems, Fault tolerance, resilience, survivability, robustness in GRID, QoS/SLA in GRID networks, GRID fora, standards, development, evolution, GRID

ISSN 1813-2065 Printed in IRAQ

case studies, validation testbeds, prototypes, and lessons learned

Computing in Virtualization-based environments

Principles of virtualization, Virtualization platforms, Thick and thin clients, Data centers and nano-centers, Open virtualization format, Orchestration of virtualization across data centers, Dynamic federation of compute capacity, Dynamic geo-balancing, Instant workload migration, Virtualization-aware storage, Virtualization-aware networking, Virtualization embedded-software-based smart mobile phones, Trusted platforms and embedded supervisors for security, Virtualization management operations /discovery, configuration, provisioning, performance, etc., Energy optimization and saving for green datacenters, Virtualization supporting cloud computing, Applications as pre-packaged virtual machines, Licencing and support policies

Computing applications in science

Advanced computing in civil engineering, Advanced computing in physics science, Advanced computing in chemistry science, Advanced computing in mathematics, Advanced computing in operation research, Advanced computing in economics, Advanced computing in electronics and electrical science, Advanced computing on Earth science, geosciences and meteorology

Complex computing in application domains

Computation genomic, Management of scientific data and knowledge, Advanced computing in bioinformatics and biophysics, Advanced computing in molecular systems and biological systems, Application of engineering methods to genetics, Medical computation and graphics, Advanced computing in simulation systems, Advanced computing for statistics and optimization, Advanced computing in mechanics and quantum mechanics, Advanced computing for geosciences and meteorology, Maps and geo-images building, Curve and surface reconstruction, Financial computing and forecasting, Advanced computing in robotics and manufacturing, Advanced computing in power systems, Environmental advanced computing

INSTRUCTION FOR THE AUTHORS

The ADVCOMP 2009 Proceedings will be published by IEEE Computer Society Press and on-line via IEEE XPlore Digital Library. IEEE will index the papers with major indexes. Authors of selected papers will be invited to submit extended versions to one of the IARIA Journals.

Important deadlines:

Submission (full paper)	May 20, 2009
Notification	June 25, 2009
Registration	July 12, 2009
Camera ready	July 15, 2009

Only .pdf or .doc files will be accepted for paper submission. All received papers will be acknowledged via an automated system.

Final author manuscripts will be 8.5" x 11" (two columns IEEE format), not exceeding 6 pages; max 4 extra pages allowed at additional cost. Your paper should also comply with the additional editorial rules. Once you receive the notification of paper acceptance, you will be provided by the IEEE CS Press an online author kit with all the steps an author needs to follow to submit the final version. The author kits URL will be included in the letter of acceptance.

Poster Forum

Posters are welcome. Please submit the contributions following the instructions for the regular submissions using the "Submit a Paper" button and selecting the track/workshop preference as "POSTER : Poster Forum". Submissions are expected to be 6-8 slide deck. Posters will not be published in the Proceedings. One poster with all the slides together should be used for discussions. Presenters will be allocated a space where they can display the slides and discuss in an informal manner. The poster slide decks will be posted on the IARIA site.

Work in Progress

Work-in-progress contributions are welcome. Please submit the contributions following the instructions for the regular submissions using the "Submit a Paper" button and selecting the track/workshop preference as "WIP: Work in Progress". Authors should submit a four-page (maximum) text manuscript in IEEE double-column format including the authors' names, affiliations, email contacts. Contributors must follow the conference deadlines, describing early research and novel skeleton ideas in the areas of the conference topics. The work will be published in the conference proceedings.

Technical marketing/business/positioning presentations

The conference initiates a series of business, technical marketing, and positioning presentations on the same topics. Speakers must submit a 10-12 slide deck presentations with substantial notes accompanying the slides, in the .ppt format (.pdf-ed). The slide deck will not be published in the conference's CD Proceedings. Presentations' slide decks will be posted on the IARIA's site. Please send your presentations to petre@iaria.org.

Tutorials

Tutorials provide overviews of current high interest topics. Proposals should be for three hour tutorials. Proposals must contain the title, the summary of the content, and the biography of the presenter(s). The tutorials' slide decks will be posted on the IARIA's site. Please send your proposals to petre@iaria.org

Panel proposals:

The organizers encourage scientists and industry leaders to organize dedicated panels dealing with controversial and challenging topics and paradigms. Panel moderators are asked to identify their guests and manage that their appropriate talk supports timely reach our deadlines. Moderators must specifically submit an official proposal, indicating their background, panelist names, their affiliation, the topic of the panel, as well as short biographies. The panel's slide deck will be posted on the IARIA's site. For more information, petre@iaria.org

Workshop proposals

We welcome workshop proposals on issues complementary to the topics of this conference. Your requests should be forwarded to petre@iaria.org.

Call For Papers

The 3rd International Conference on Bioinformatics and Biomedical Engineering (iCBBE 2009)

June 11-13, 2009 Beijing, China

The 3rd International Conference on Bioinformatics and Biomedical Engineering (iCBBE 2009) will be held from June 11th to 13th, 2009 in Beijing, China. iCBBE 2009 will bring together top researchers from Asian Pacific areas, North America, Europe and around the world to exchange research results and address open issues in all aspects of bioinformatics and biomedical engineering. As we did in iCBBE 2008 and 2007, all accepted papers in iCBBE 2009 will be published by IEEE and indexed by EI Compendex.

Topics

Bioinformatics and Computational Biology

- Protein structure, function and sequence analysis
- Protein interactions, docking and function
- Computational proteomics
- DNA and RNA structure, function and sequence analysis
- Gene regulation, expression, identification and network
- Structural, functional and comparative genomics
- Gene engineering and protein engineering
- Computational evolutionary biology
- Drug design and computer aided diagnosis
- Data acquisition, normalization, analysis and visualization
- Algorithms, models, software, and tools in Bioinformatics
- Any novel approaches to bioinformatics problems

Biomedical Engineering

- Biomedical imaging, image processing & visualization
- Bioelectrical and neural engineering
- Biomaterials and biomedical optics
- Biomechanics and bio-transport
- Methods and biology effects of NMR/CT/ECG technology
- Biomedical devices, sensors, and artificial organs
- Biochemical, cellular, molecular and tissue engineering
- Biomedical robotics and mechanics
- Rehabilitation engineering and clinical engineering
- Health monitoring systems and wearable system
- Bio-signal processing and analysis
- Biometric and bio-measurement
- Other topics related to biomedical engineering

Conference Organizing Committee

- Dr. K. C. Chou (Gordon Life Science Institue, USA),Chair
- Dr. W. Kainz (Food and Drug Administration, USA)
- Dr. J. Chen (University of Houston, USA)
- Dr. F. C. He (Chinese Academy of Science,China)
- Dr. H. B. Zhou (Wuhan University, China)
- Dr. T. Casavant (University of Iowa, USA)
- Dr. J. Zhang (University of Kentucky, USA)

Sponsors

- IEEE Eng. in Medicine and Biology Society, USA
- Gordon Life Science Institute, USA
- Fudan University, China
- Beijing Institute of Technology, China
- Wuhan University, China
- University of Iowa, USA
- Food and Drug Administration, USA
- Journal of Biomedical Science and Engineering

Important Dates

- Papers Due: Nov. 30, 2008
- Acceptance Notification: Feb. 10, 2009
- Conference: June 11-13, 2009

Contact Information

Website:http://www.icbbe.org
E-mail: submit@icbbe.org

A New Fractal Microstrip Bandpass Filter Design Based on Dual-Mode Square Ring Resonator for Wireless Communication Systems

Jawad K. Ali
Nasr N. Husain

Department of Electrical and Electronic Engineering, University of Technology, P. O. Box 35239, Baghdad, IRAQ

A new fractal design scheme has been introduced to generate dual-mode microstrip bandpass filter designs with miniaturized sizes for wireless applications. The presented fractal scheme is based on the Koch pre-fractal geometry applied to the conventional dual-mode microstrip square ring resonator as an initiator in the fractal generation process. The space-filling property that the proposed structures possesses, was found to produce reduced size symmetrical structures corresponding to the successive iteration levels. In addition, self-similarity of the whole structure about its diagonal, at any iteration level, enables it to produce the two degenerate modes which can then be coupled using a proper perturbation technique. These filter designs are of sizes suitable for use in modern wireless communication systems. The performance of each of the generated bandpass filter structures up to the 2^{nd} iteration has been analyzed using a method of moments (MoM) based software IE3D, which is widely adopted in microwave research and industry. Results show that these filters possess good transmission and return loss characteristics, besides the miniaturized sizes gained; meeting the design specifications of most of wireless communication systems.

***Keywords*:** Microstrip filter, Koch fractal, filter miniaturization, dual-mode resonator
Received: 8 November 2008, **Revised**: 18 January 2009, **Accepted**: 25 January 2009

1. Introduction

Fractal geometry has found extensive applications in almost all the fields of science, technology and art, since the pioneering work of Mandelbrot about three decades ago [1]. Among these fields are the physical and engineering applications. In electromagnetics, fractal geometry has been applied widely in the fields of antenna and passive microwave circuit design, due the fantastic results gained in the miniaturization and the performance as well.

Two common properties; space-filling and self-similarity, that fractal geometries have, make them different from Euclidean geometries. It has been shown that the self-similarity property of fractal shapes can be successfully applied to the design of multi-band fractal antennas, such as the Sierpinski gasket antenna [2], while the space-filling property of fractals can be utilized to reduce antenna size [3]. Fractal curves are well known for their unique space-filling properties. Research results showed that, due to the increase of the overall length of the microstrip line on a given substrate area as well as to the specific line geometry, using fractal curves reduces resonant frequency of microstrip resonators, and gives narrow resonant peaks. Most of the research efforts has been devoted to antenna applications. In passive microwave design, the research is still limited to few works and is slowly growing [2,3]. Among the earliest predictions of the use of fractals in the design and fabrication of filters is that of Yordanov et al., [4]. Their predictions are based on their investigation of Cantor fractal geometry.

However, recent development in wireless communication systems has presented new challenges to design and production of high-quality miniaturized components. These challenges stimulate microwave circuits designers and antenna designers to seek out for solutions by investigating different fractal geometries [5-9]. Hilbert's fractal curve has been used as a defected ground structure in the design of a microstrip lowpass filter operating at the L-band microwave frequency [5]. Sierpinski fractal geometry has been used in the implementation of a complementary split ring resonator [6]. Split ring geometry using square Sierpinski fractal curves has been proposed to reduce resonant frequency of the structure and achieve improved frequency selectivity in the resonator

performance [8]. Koch fractal shape is applied to mm-wave microstrip bandpass filters integrated on a high-resistivity Si substrate [9]. Results showed that the 2nd harmonic of fractal shape filters can be suppressed as the fractal factor increases, while maintaining the physical size of the resulting filter design [7]. Minkowski-like prefractal geometry has been used successfully in producing high performance miniaturized dual-mode microstrip bandpass filters [2,3].

In this paper, a new fractal scheme, based on applying Koch pre-fractal curve to the conventional microstrip dual-mode square ring resonator, is used to produce successful miniaturized design structures for the dual-mode microstrip bandpass filter. The resulting dual-mode bandpass filters are supposed to have noticeably miniaturized sizes with adequate reflection and transmission responses.

2. The Proposed Fractal Scheme

The square ring with a side length L_o, Fig. (1b), is considered as the starting pattern for the proposed bandpass filter as a fractal. From this starting pattern, each of its four sides is replaced by what is called the generator structure shown in Fig. (1a). To demonstrate the fractal generation process, the first two iterations are shown. The first iteration of replacing a segment with the generator is shown in Fig. (1c). The starting pattern is Euclidean and, therefore, the process of replacing the segment with the generator constitutes the first iteration. The generator is scaled after, such that the endpoints of the generator are exactly the same as the starting line segment. In the generation of the true fractal, the process of replacing every segment with the generator is carried out an infinite number of times. The resulting pre-fractal structure has the characteristic that the perimeter increases to infinity while maintaining the volume occupied. This increase in length decreases the required volume occupied for the pre-fractal bandpass filter at resonance. It has been found that [4,5]:

$$P_n = \left(\frac{4}{3}\right)^n P_{n-1} \qquad (1)$$

where P_n is the perimeter of the n^{th} iteration pre-fractal structure. Theoretically, as n goes to infinity the perimeter goes to infinity. The ability of the resulting structure to increase its perimeter in the successive iterations was found very promising for examining its size reduction capability as a microstrip bandpass filter.

The basic idea to propose this fractal technique to generate a miniaturized microstrip bandpass filter structures has been borrowed from the successful application of such a technique in the microstrip antenna design, where compact size and multi-band behavior have been produced due to the space-filling and self-similarity properties of the resulting microstrip fractal antenna design [2,3,10-12].

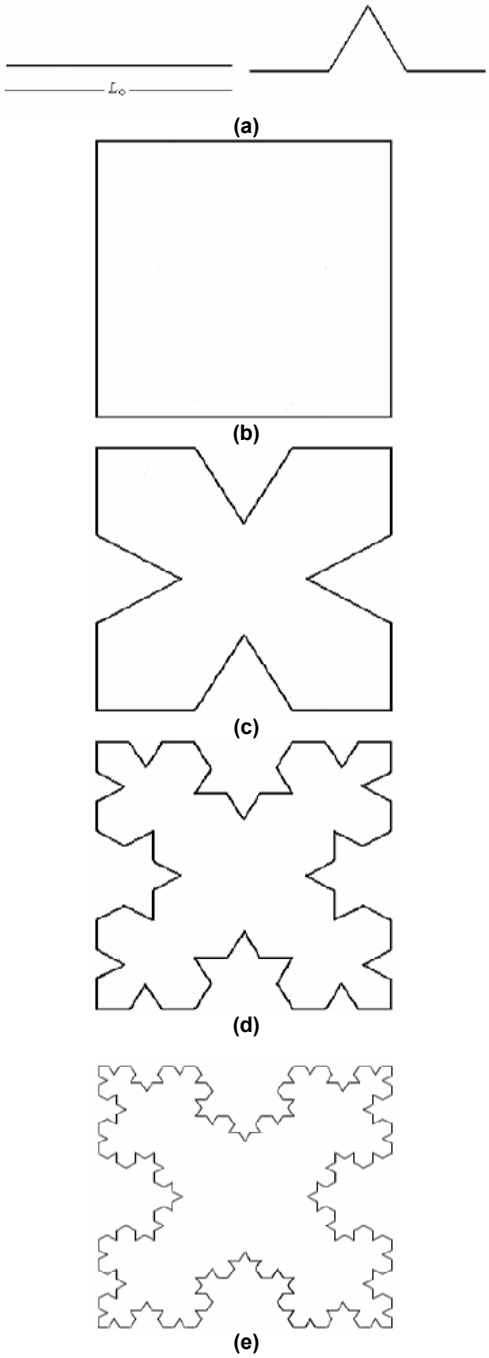

Fig. (1) The generation process of the Minkowski-like prefractal structure; (a) the generator, (b) the square ring resonator, (c) the 1st iteration, (d) the 2nd iteration, and (e) the 3rd iteration

It has been concluded in antenna design, that the number of generating iterations required to make use of the benefits of miniaturization is only few before the additional complexities become indistinguishable [10,13]. This is true in this field, since the antenna aperture when much reduced leads to less gain though the radiation performance is still attractive. However, this

cannot be as serious in the filter design unless practical limitations obscure its implementation due to fabrication tolerances.

In practice, shape modification of the resulting structures in Figs. (1c) and (1d) is a way to increase the surface current path length compared with that of the conventional square ring resonator, Fig. (1b); resulting in a reduced resonant frequency or a reduced resonator size, if the design frequency is to maintain. It is expected then, that the 2nd iteration, shown in Fig. (1d) will exhibit further miniaturization ability owing to its extra space filling property. Theoretically, the size reduction process goes on further as the iteration steps increase. An additional property that the presented scheme possesses is the symmetry of the whole structure in each of the iteration levels about its diagonal. This property is of special importance in the design of dual-mode loop resonators [14,15].

The length L_o of the conventional microstrip dual-mode square ring resonator has been determined using the classical design equations reported in the literature [14-16] for a specified operating frequency and given substrate properties. This length represents a slightly less than the quarter guided wavelength at its fundamental resonant frequency in the resonator.

Applying geometric transformation of the generating structure (Fig. 1a) on the square ring resonator (Fig. 1b), results in the filter structure depicted in (Fig. 1c). Similarly, successive bandpass filter shapes, corresponding to the subsequent iterations, can be produced as successive transformations are applied. At the n^{th} iteration, the corresponding pre-fractal enclosing area, A_n has been found to be [4,5]:

$$A_n = \left(1 - \frac{2^{2n-1}}{3^{2n}}\right) A_{n-1} \qquad (2)$$

The dimension of a fractal provides a description of how much it efficiently fills a space. It is a measure of the prominence of the irregularities when viewed at very small scales [17,18]. A dimension contains much information about the geometrical properties of a fractal. From the property of self-similarity, the fractal dimension D is defined as [17]:

$$D = \frac{\log(N)}{\log(1/r)} \qquad (3)$$

where N is the total number of distinct copies and $1/r$ is the scale ratio

To find the dimension of the Koch fractal curve, using Eq. (3), where N=4 segments and r=1/3, then the fractal dimension is D=1.26.

3. Filter Design

Three dual-mode microstrip bandpass filter structures corresponding to the zero, 1st, and 2nd iterations have been designed for the ISM band applications at a design frequency of 2.4GHz. It has been supposed that these filter structures have been etched using a substrate with a dielectric constant of 10.8 and thickness of 1.27mm. At first, the side length of the square ring resonator, L_o, has to be calculated as [14-16]:

$$L_0 < \frac{\lambda_{go}}{4} \qquad (4)$$

where λ_{go} is the guided wavelength. Then the side length, L_n, for the successive iterations can be calculated, based on the value of L_0, using Eq. (1).

A small perturbation has been applied to each dual-mode resonator at a location that is assumed at a 45° offset from its two orthogonal modes. This perturbation, in the form of a small patch, is added to the square ring, and to the other subsequent iterations loop resonators. It should be mentioned that for coupling of the orthogonal modes, the perturbations could also take forms and locations other than the mentioned shape and position. But since the resulting resonators are characterized by their diagonal symmetry, this shape of perturbation is the most convenient to satisfy the required coupling. The effect of the perturbation size on the dual-mode ring resonator filter performance curves is not discussed here; since the main aim is to present a new technique for generating miniaturized bandpass filter design based on a fractal iteration process with acceptable performance. The dimensions of the perturbations of each filter must be tuned to satisfy the required filter performance, since the nature and the strength of the coupling between the two degenerate modes of the dual-mode resonator are mainly determined by the perturbation's size and shape. However, extensive details about this subject can be found in [19,20].

The initially calculated value of L_o has to be adjusted to the design frequency, therefore, slight tuning of this value is necessary. Figures (2) and (3) show the layouts of the resulting dual-band bandpass filters and Table (1) summarizes the resulting side lengths and the satisfied size reduction percentages as compared with the conventional square ring resonator at the design frequency. It is expected that the 3rd and the 4th iterations bandpass filter structures may satisfy further size reductions of about 82% and 89% respectively, if the fabrication tolerances permit implementation.

ISSN 1813-2065

4. Performance Evaluation

Filter structures, depicted in Figs. (2) and (4), have been modeled and analyzed at an operating frequency, in the ISM band, of 2.4GHz using the IE3D electromagnetic simulator from Zeland Software Inc. [21]. This simulator performs electromagnetic analysis using the method of moments (MoM). The corresponding simulation results of return loss and transmission responses of these filters are shown in Figs. (5) and (7), respectively.

Table (1) Summary of the dimensions and the size reduction percentages of the pre-fractal filters up to 4th iteration at a design frequency of 2.45GHz

Filter Type	L_n (mm)	Size Reduction (%)
Square patch (0 iteration)	41.35	-
1st iteration	31.01	43.75
2nd iteration	23.25	68.38
3rd iteration	17.44	82.21
4th iteration	13.08	89.98

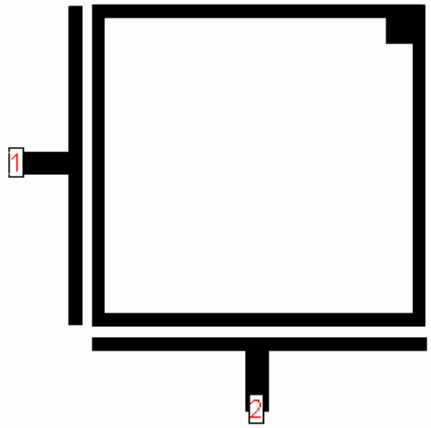

Fig. (2) The layout of the dual-mode microstrip square ring resonator

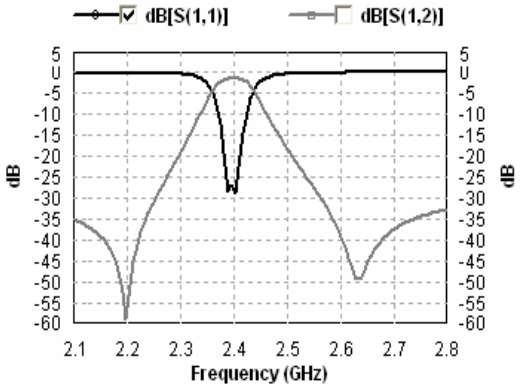

Fig. (3) The return loss and transmission responses of the dual-mode microstrip square ring resonator

It is implied from these figures that the resulting pre-fractal bandpass filters offer adequate performance curves as those for the conventional dual-mode square ring resonator, Fig. (5). As can be seen, all of the filter responses show two transmission zeros symmetrically located around the deign frequency.

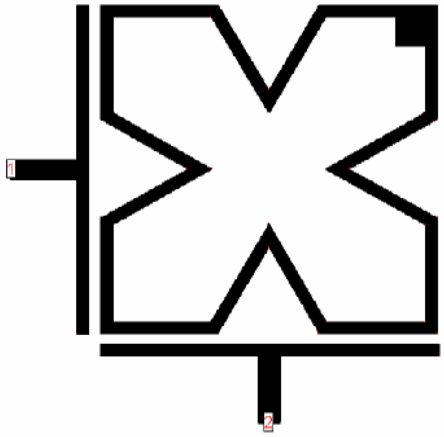

Fig. (4) The layout of the resulting dual-mode 1st iteration fractal microstrip bandpass filter

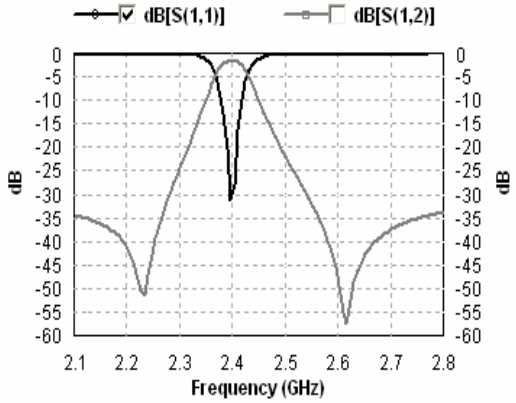

Fig. (5) The return loss and transmission responses of the resulting dual-mode 1st iteration fractal microstrip bandpass filter

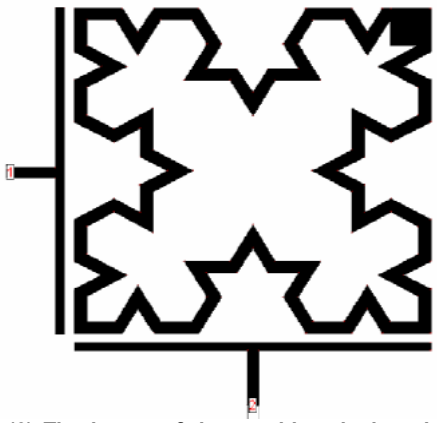

Fig. (6) The layout of the resulting dual-mode 2nd iteration fractal microstrip bandpass filter

However, these responses and their consequent poles and zeros could be, to a certain extent, controlled through the variation of the perturbation dimensions and/or the input/output coupling used. Figures (8-10) show the current density patterns using the EM simulator for 2nd iteration dual-mode microstrip bandpass filter at

the design frequency and other two frequencies around it.

It clear from these figures that only at the design frequency the two degenerate modes are excited and coupled to each other leading to the required filter performance, while at the other two frequencies, no degenerate modes are excited at all as expected. In these figures, the same color code is used as an indication for the current densities.

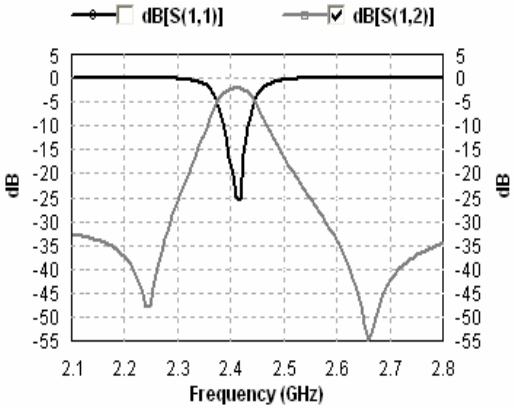

Fig. (7) The return loss and transmission responses of the resulting dual-mode 1st iteration fractal microstrip bandpass filter

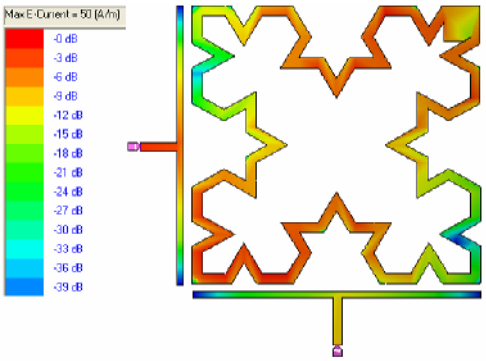

Fig. (8) Current density distribution at the surface of the 2nd iteration microstrip bandpass filter simulated below resonance at a frequency of 2.35 GHz

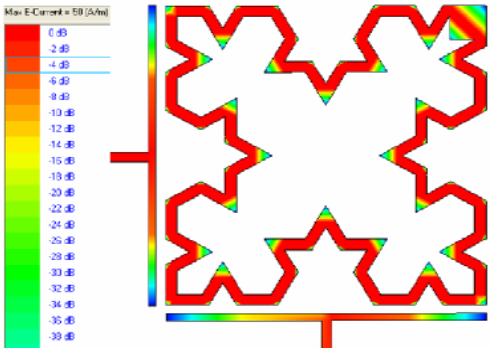

Fig. (9) Current density distribution at the surface of the 2nd iteration microstrip bandpass filter simulated at resonant frequency of 2.4GHz

The previous filter designs can easily be scaled to other frequencies required for other wireless communication systems. In this case, the resulting new filter will be of lager or smaller size according to the frequency requirements of the specified applications.

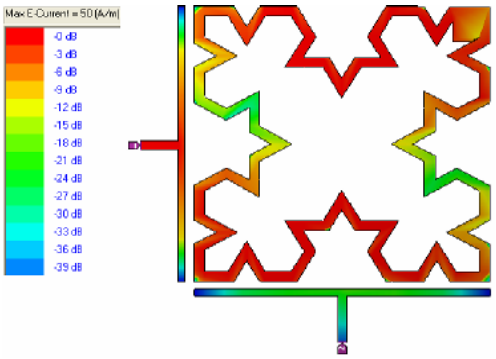

Fig. (10) Current density distribution at the surface of the 2nd iteration microstrip bandpass filter simulated above resonance at a frequency of 2.55 GHz

5. Conclusions

A fractal design scheme has been presented in this paper, as a new technique for microstrip bandpass filter design based on dual-mode square ring resonator. Due to the space-filling property of the presented fractal possess, the resulting filter designs have proven to be more compact in size as the iteration process goes on. This makes them appropriate for use in modern mobile communication systems, where the miniaturized size becomes a critical requirement.

Up to the 2nd iteration, microstrip bandpass filters have been designed according to the presented technique and analyzed using the method of moments (MoM) at the ISM frequency band. Simulation results show that these filters possess reasonable return loss and transmission performance responses.

Microstrip bandpass filters designs based on the 1st and 2nd iterations have shown size reductions of about 43% and 68% as compared with the conventional microstrip square ring bandpass filter designed at the same frequency and using the same substrate material. As the practical fabrication tolerances may permit, it is expected that the 3rd iteration and 4th iteration filter structures will offer further size reductions of about 82% and 89% respectively, as predicted by the presented fractal scheme.

The proposed technique can be generalized, as a flexible design tool, for compact microstrip bandpass filters for a wide variety of wireless communication systems.

References

[1] B.B. Mandelbrot, "**The fractal Geometry of Nature",** W. H. Freeman and Company (New York) (1983) 25.
[2] J.K. Ali, "Fractally Generated Microstrip Bandpass Filter Designs Based on Dual-Mode Square Ring Resonator for Wireless Communication Systems", *Proc. of the 2nd Al-Khawarizmi Eng. Conf., Univ. of Baghdad* (Baghdad, Iraq), April 22-23, 2008.
[3] J.K. Ali, "A New Miniaturized Fractal Bandpass Filter Based on Dual-Mode Microstrip Square Ring Resonator", *Proc. of the 5th Inter. Multi-Conf. on Signals, Systems and Devices, IEEE SSD '08* (Amman, Jordan), July 20-23, 2008.
[4] O.I. Yordanov et al., "Prospects of Fractal Filters and Reflectors," *IEE 7th Inter. Conf. on Antenna and Propagation, ISCAP91* (York, UK) (1991), 698-700.
[5] J. Chen et al., *Prog. in Electromag. Res., PIER,* 70 (2007) 269-280.
[6] V. Crnojevic-Bengin, V. Radonic, and B. Jokanovic, "Complementary Split Ring Resonators Using Square Sierpinski Fractal Curves", *Proc. of the 36th European Microwave Conf.* (Manchester, UK) (2006), 1333-1335.
[7] I.K. Kim et al., *J. Kor. Electromag. Eng. Soc., JKEES,* 6(4) (2006) 1-10.
[8] J.K. Xiao, Q.X. Chu and S. Zhang, *Prog. in Electromag. Res., PIER,* 77 (2007) 343-356.
[9] G.L. Wu et al., *Prog. in Electromag. Res., PIER,* 78 (2008) 17-24.
[10] J.K. Ali, *J. Eng. Appl. Sci., JEAS,* 2(7) (2007) 1120-1124.
[11] J.K. Ali and A.S. Jalal, *Asian J. Infor. Technol., AJIT,* 6(5) (2007) 584-588.
[12] J.K. Ali, *Univ. of Babylon J. Sci. (printed in Iraq),* 16(1) (2008) 555-543.
[13] J.P. Gianvittorio, "Fractals, MEMS, and FSS Electromagnetic Devices: Miniaturization and Multiple Resonances", Ph.D. thesis, University of California (U.S.A) (2003) 8.
[14] L. Hsieh and K. Chang, *IEEE Trans. Microwave Theory Tech.,* 28(8) (1980) 1141–1145.
[15] K. Chang and L.H. Hsieh, **"Microwave Ring Circuits and Related Structures",** 2nd ed., John-Wiley & Sons Ltd., (NJ) (2004) 56.
[16] J.S. Hong and M.J. Lancaster, **"Microstrip Filters for RF/Microwave Applications",** John-Wiley & Sons Inc., (NY) (2001) 407.
[17] K. Falconer, **"Fractal Geometry; Mathematical Foundations and Applications",** 2nd ed., John-Wiley & Sons Ltd., (Chichester) (2003) 27.
[18] H. Peitgen, H. Jürgens, D. Saupe, **"Chaos and Fractals,"** New Frontiers of Science, 2nd ed., Springer-Verlag (NY) (2004) 173.
[19] A. Görür, *IEEE Trans. Microwave Theory Tech.,* 52(2) (2004) 671-677.
[20] S. Amari, *IEEE Trans. Microwave Theory Tech.,* 52(9) (2004) 2190-2192.
[21] Zeland's IE3D, Release 14.1, Zeland Software, Inc., Fremont, CA, May 2008.

CALL FOR PAPERS

IEEE Journal on Selected Areas in Communications
Optical Communications and Networking Series

THE ROLE OF OPTICAL AND ELECTRONIC TECHNOLOGIES FOR LARGE CAPACITY SWITCHES AND ROUTERS

Next-Generation Networks will have to support a range of services and access technologies. The evolution of broadband wireless access technologies, such as HSPA and WiMax, and wireline technologies such as FTTx and advanced HFC, are providing the means to support the massive amount of traffic related to quadruple-play services, including peer-to-peer, voice and video, new Internet services, and IPTV. The ever-increasing volume of traffic at the network edge is now posing challenging requirements for the core network infrastructure. As a result, there will soon be a need for high-capacity switches (e.g., L2) and routers that can handle throughputs of tens of terabits per second. Future traffic growth may eventually push switch/router capacities to hundreds of terabits per second. A very serious limitation on capacity growth in today's electronic routers is energy consumption and the associated issue of heat dissipation. Removing heat from the equipment racks and from the building in which the racks are housed is becoming a major engineering challenge. Also at issue is the growing footprint of an expanding number of racks of equipment in telco offices.

In this environment, it is crucial to investigate solutions and technologies that will allow the realization of new generations of switches and routers, which address key problems such as scalability to increasing bit rates and increasing number of interfaces, high-speed inter-board and inter-rack interconnections, equipment packing density, and above all, power consumption and heat dissipation.

In the last two decades, various switching approaches using photonics have appeared in the technical literature. Examples include all-optical packet switching (OPS), all-optical burst switching (OBS) and optical flow switching (OFS). However, after many years of research on these approaches in many laboratories, key problems remain unsolved. For example, there is currently no viable all-optical technology for buffering packets, there has been no practical demonstration of an optical cross connect that can switch at the speed required for packet switching and, at the same time, scale to the capacity required for future network applications. Most importantly, it remains unclear whether optical technologies can solve the critically-important energy consumption problem. A more likely scenario is that future switches and routers will incorporate a combination of electronic and optical technologies. For example, new optical approaches to switching might be able to replace some or all of the electronic switch fabric.

The objective of this Special Issue is to provide a focus for manuscripts describing work that helps to define the roles of electronics and optics in future high-capacity routers. To this end, we solicit original manuscripts relating to how high-capacity switches and routers can be realized, through a wise combination of electronic, photonic, and optoelectronic technologies.

Researchers and technology experts from both Industry and Academia are invited to submit original work on topics within this scope, including the following:

- High-capacity switch/router architectures
- High-speed switching fabric architectures and related technologies
- Hybrid electronic/optical switching
- Optical vs. electronic solutions for the realization of switching and mux/demux
- Solutions for addressing scalability, cost, and, particularly, power consumption
- Performance of high-capacity switches and routers
- Network architectures that enable more scalable switch/router sizes
- Buffer sizing for routers, including architectures and protocols that reduce the required buffer size
- High-speed interconnects
- New electronic/optic components for switching and routing such as buffers and header processors
- Nanophotonics for switching and routing
- Low-power integrated optical circuits
- Energy source impact on network architecture and design

Authors should follow the IEEE J-SAC manuscript format described in the Information for Authors (http://www.argreenhouse.com/society/J-SAC/Guidelines/info.html). Prospective authors should submit a pdf version of their complete manuscript via email to one of the Guest Editors according to the following timetable:

Manuscript Submission:	April 3, 2009
Acceptance Notification:	April 30, 2009
Final Manuscript Due:	June 30, 2009
Publication:	August 2009

Guest Editors

Ken-ichi Kitayama (kitayama@comm.eng.osaka-u.ac.jp), Rodney Tucker (r.tucker@ee.unimelb.edu.au), and Roberto Sabella (roberto.sabella@ericsson.com), JSAC Part 2 editors: Ori Gerstel, Jane Simmons.

ISSN 1813-2065

Preliminary Announcement

2009 International Conference on Solid State Devices and Materials (SSDM 2009)

Date: October 6-9, 2009 (Short Course & Workshop: October 6, 2009)
Place: Sendai Kokusai Hotel, Sendai, Japan

The 2009 International Conference on Solid Sate Devices and Materials (SSDM2009) will be held from October 6, Tuesday, through October 9, Friday, at Sendai Kokusai Hotel, Sendai, Japan.

This conference is one of the most important and prestigious international conferences held in Japan. The SSDM has provided a good opportunity to present and discuss key aspects of solid state devices and materials since it started in 1969. From 1999 conference, program sub-committees have been established to further advance the SSDM conference activity. This organizational change has led to higher quality paper selection, which results in a higher level of presentations and discussions in the various potential subject areas. The conference has 10 sub-committees in Core Areas and 4 sub-committees in Strategic Areas, as shown below, which are continuously focused on pointing our the future directions in solid state devices and materials research. In addition to the main conference program, one-day short courses and workshop programs will precede the conference on Tuesday, October 6, which offer tutorial lectures on interesting topics.

Papers will be solicited in the following areas (=Subcommittees) for SSDM2009

Core Areas

I : Advanced Gate Stack / Si Processing Science
II : Characterization and Materials Engineering for Interconnect Integration
III : CMOS Devices /Device Physics
IV : Advanced Memory Technology
V : Advanced Circuits and Systems
VI : Compound Semiconductor Circuits, Electron Devices and Device Physics
VII : Photonic Devices and Device Physics
VIII : Advanced Material Synthesis and Crystal Growth Technology
IX : Physics and Applications of Novel Functional Materials and Devices
X : Organic Materials Science, Device Physics, and Applications

Strategic Areas

XI : Micro/Nano Electromechanical and Bio-Systems (Devices)
XII : Spintronic Materials and Devices
XIII : Applications of Nanotubes and Nanowires
XIV : Power Electronics

※CONFERENCE LANGUAGE
The official language of the conference is English.

IMPORTANT DATES

First Announcement	December, 2008
Second Announcement	March, 2009
Deadline for Abstracts	May 8, 2009
Deadline for Late News Papers	July 27, 2009

CONFERENCE CHAIRS

Organizing Committee Chair
Mitsumasa Koyanagi (Tohoku Univ.)

Steering Committee Chair
Seiji Samukawa (Tohoku Univ.)

Program Committee Chair
Kazumi Wada (Univ. of Tokyo)

FURTHER INFORMATION

Those who are interested in receiving further information, including the call for papers, are requested to contact:
Secretariat for SSDM 2009
c/o Inter Group Corp.
Phone: +81-3-3597-1108 Fax: +81-3-3597-1097 E-mail: ssdm_secretariat@intergroup.co.jp
URL: http://www.ssdm.jp

ISSN 1813-2065

Torque and Magnetic Flux Analysis Using an Advanced Dynamic Dynamometer Test Bed for Electromechanical Motors

Jamal M. Al-Baiaty
Naseer F. Daoud
Hani G. Khayat

Department of Mechanical Engineering, College of Engineering, University of Kirkuk, Krkuk, IRAQ

This paper describes the torque and magnetic flux analysis using an advanced dynamic dynamometer test bed for electromechanical motors. Test motor was tested under different levels of continuous loads and high bandwidth complex duty cycle loads in order to provide data to characterize the nonlinear properties of electric motors. The test bed to obtain torque saturation limit data is comprised of a servo motor which serves as a dynamic load emulator, a brake, a clutch, and full sensor array for comprehensive monitoring of test variables, (including magnetic flux density sensor). The magnetic flux test was conducted to discriminate magnetic saturation from torque saturation. Given the permanent magnet motor test system designed for a desired saturation limit, it is possible to predict saturation using a properly defined dynamic duty cycle norm as a function of the operating conditions and the actuator design parameters. In this paper, the temperature effects on the magnetic properties of the permanent magnet material were the principal objectives.

Keywords: Motion control, Electromechanical motor, Torque, Magnetic saturation
Received**: 16 December 2008,** Revised**: 18 January 2009,** Accepted**: 25 January**

1. Introduction

The development of high energy magnets is an area of major interest in permanent magnet actuation technology. Attention has been particularly focused on Permanent Magnet Synchronous Motors (PMSM) and Brushless DC Motors (BDCM). However, PMSM and BDCM have not replaced conventional DC motors or induction motors as fast as anticipated. This is due to several manufacturing issues associated with these types of motors. The foremost concern is the possibility of torque saturation. Neodymium-iron-boron (Nd-Fe-B) permanent magnets, which are the most commonly used permanent magnet for industrial motors, saturate at temperatures above $150°C$. This effect limits the use of both PMSM and BDCM in applications such as robotics, industrial machines, space engineering, and demanding manufacturing environments. In order to avoid the saturation phenomenon at high temperatures, a careful design of the motor with a judicious selection of components must be made. This paper examines temperature effects on the torque production capability of PM motors equipped with Nd-Fe-B magnets.

The paper explains the process for determining the torque saturation limit for a PM motor under heavy loads at elevated temperatures. Then, based on the well-understood mechanism for magnetic saturation during operation of the stator and rotor, a torque saturation limit can be induced. Most motor users are more interested in the torque output saturation, which is different from magnetic saturation. The motor parameters change due to the effect of the magnetic saturation, and as a result, the output performance of the motor is affected. After a brief review of a general permanent magnet motor, models for torque generation, overall review of actuator test bed and magnetic saturation are presented.

2. Background

2.1 General Permanent Magnet Motor

In permanent magnet actuation technology, there are two kinds of motors, Permanent Magnet Synchronous Motor (PMSM) and Brushless DC Motor (BDCM). The difference between them is in the shape of the back EMF. That is, the PMSM has a sinusoidal back EMF while the BDCM has a trapezoidal back EMF [1]. This paper focuses on the model of a PMSM. This motor consists of a steel rotor, a position sensor mounted on the rotor, an electronic circuitry, a logic controller, and a stator [2]. The steel rotor has the strips of permanent magnets mounted on its surface. These magnets create magnetic fields that interact with the magnetic fields produced in the stator windings to generate torque. The

position sensor, which is connected to the stator, is generally either an encoder or a resolver. This sensor provides accurate information about the angular position of the rotor, which is used in the commutation of the currents in the stator windings. The electronic circuitry commutates the currents in the stator windings according to control signals provided by a logic controller. This controller sends low voltage signals to the electronic circuitry to produce the commutation of the currents in the stator windings. The controller uses the angular position provided by the position sensor to produce the torque demanded by the actuator. Finally, the stator is constructed with three phases, generally Y-connected. The constant switching of the currents in the phases of the stator produces a constant torque in the rotor of the motor.

A set of first order differential equations that explains the dynamic behavior of a PMSM can be obtained as in [3]. This set can be simplified by using a general mathematical transformation known as the d-q transformation. Basically, the d-q transformation uses the properties of trigonometric identities to remove the sinusoidal terms that appear in the equations due to the back EMF. The simplified set of equations, known as d-q equations, is simpler to use than the original set as shown in Eq. (1)

$$\begin{aligned} \frac{di_q}{dt} &= -\frac{R}{L-M} i_q - n\, i_d \omega - \frac{-n\, k_e}{L-M}\omega + \frac{1}{L-M} v_q \\ \frac{di_d}{dt} &= -\frac{R}{L-M} i_d + n\, i_q \omega + \frac{1}{L-M} v_d \end{aligned} \quad (1)$$

where i_q is the current in quadrature-axis, i_d is the current in the direct-axis, v_q is the voltage in the quadrature-axis, v_d is the voltage in the direct-axis, ω is the speed of the test motor, n is the number of pole pairs in the PMSM, L and M are the self and mutual inductances of the coils, R is the resistance in each phase, and k_e is the electromotive force constant. The subscripts, q, d, represent the variables associated with fictitious windings rotating with the rotor of the motor. Park's transformation was used to convert the real winding axis to a rotating frame with the rotor of the motor [4,22].

However, the set of equations was obtained under the assumption that the flux linkage and the currents in the phases are linearly related. In the presence of magnetic saturation, this assumption is not valid. The flux linkage terms in the set of equations are no longer linear functions of the currents and the angular position of the rotor. Therefore, a new set of equations that takes into account this condition should be obtained to explain the dynamic behavior of the motor under the saturation phenomenon. Previous efforts [3,5] have been made to obtain the nonlinear relations of the flux linkage, the currents, and the angular position. In this paper, based on the full explanation of the mechanism of magnetic saturation, the torque saturation limit is induced. Recall that most motor users are more interested in the torque output saturation, which is different from magnetic saturation.

2.2 Torque Equation and Model

Torque is calculated by differentiating the co-energy with respect to rotor angle. Based on this concept, one expression for the electromagnetic torque produced by a machine is given by [6]

$$\tau = \frac{3}{2}\frac{n}{2}\left(\lambda_d i_q - \lambda_q i_d\right) \quad (2)$$

where n is the number of the stator poles, and the quantities λ_d and λ_q are the direct axis and quadrature axis magnetic flux linkages, respectively. The torque is commanded in the stator flux reference frame by controlling the stator flux magnitude and the components of stator currents. Also, it shows that Eq. (2) is valid even when the motor is magnetically saturated [7]. This result is in general conformity with torque production from interacting magnetic fields as expressed in Eq. (4).

The magnitude of the charge on the particle and the magnitude of the $\vec{B}$ field as well as the velocity of the particle determine the force, $\vec{F}$, in a magnetic field. If we describe this equation in terms of the current density, $\vec{J}$, in which case the force is a force density [6]

$$\vec{F} = \vec{J} \times \vec{B} \qquad \text{N/m}^2 \quad (3)$$

This is the force density acting on the rotor magnet material itself. In order to use this equation in the electrical and magnetic field, the complex motor mechanism should be simplified with some assumptions such as the number of equilateral slots, constant and uniform air gap length, negligible armature reaction, symmetric stator currents and the stator windings [6]. Also, most electromechanical energy conversion devices are made up of rigid, non-deforming structures. In this kind of device, the net force or torque is the most important parameter.

Various techniques are used to calculate the net force and torque in the motor. In this paper, Eq. (3) is used to express the torque output in the PMSM. Slemon introduces a model of the torque by applying Eq. (4) as [7],

$$\tau = 2\pi r^2 lBJ \qquad \text{N.m} \quad (4)$$

where r is the mean radius of magnetic rotor and l is the rotor length. The root mean square value of magnetic flux density is B [Wb/m^2], and the root mean square value of current density is J [A/m]. The stator is fitted to three phase windings with the turns of each phase sinusoidally distributed. The rotor consists of an iron core with surface-mounted magnets fixed to the core. These magnets produce a radial directed average flux density in the air gap. The lumped

parameters come from the geometry of the motor constraints. The detailed explanation of Eq. (4) is described in [7] and this equation will be used to determine the torque saturation limit. Also, Hoang et al. [8] introduce their torque equation in the function of a product of magnetic flux density and current. From these expressions of torque equation, we can generalize motor torque output equation including terms of magnetic flux density and current.

2.3 Magnetism in the Motor

2.3.1 Magnetization

The quantities used to describe the strength of a magnetic field are the magnetic flux, ϕ, in units of webers (Wb) and the magnetic flux density, B, in units of webers per square meter (Wb/m^2), or Teslas (T). Magnetic field strength, or magnetizing force, H, in units of ampere per meter (A/m), is a current to generate magnetic flux density. Also, it is a physical property to measure the magnetization of the ferromagnetic material. Magneto-motive force (mmf) is defined by the total current (Ni) encircling the flux path. N is the total number of wound coils. The unit of magneto-motive force, F, is often called an ampere-turn. Magnetic reluctance, R, also can be defined by the constant of proportionality between magnetic flux, ϕ, and magneto-motive force, F [6,12,13]. When a material is placed in a magnetic field with strength, H, the interaction between the external and internal atomic moments increases the resultant flux density, B. If the induced magnetism is denoted by the magnetic moment density or magnetization, M, the flux density due to M alone is given by $B=\mu_0 M$ where the magnetic constant, μ_0, has a value of $\mu_0=4\pi x10^{-7}$H/m in SI units. The total flux density due to M and the external field, H, is $B=\mu_0 M+\mu_0 H$. Slemon and Parker [12,13] define magnetic susceptibility, χ, as the ratio of magnetization, M, and magnetic filed strength, H. Therefore, the total flux density becomes

$$B = \mu_o(x+1)H = \mu_o\mu_r H = \mu H \qquad (5)$$

where μ_r is the relative permeability of the material to free space and μ refers to the permeability of the material.

2.3.2 Ferromagnetism

If an iron core of identical dimensions replaces a free space, the total flux produced by the same coil current is enormously increased. This increase is due to the phenomenon of ferromagnetism. It is a very important factor in the process of energy conversion by electromagnetic machines like motors. The direction of alignment of the magnetic moments in a ferromagnetic material is normally along the magnetized direction. It has been shown experimentally that a specimen of ferromagnetic material is divided into so-called magnetic domains, usually of microscopic size, in each of which the atomic moments are aligned. The alignment direction differs from one domain to another [12]. Figure (1) shows ferromagnetic domains.

When a ferromagnetic material is placed in a magnetic field, the magnetic moments of the atoms tend to rotate into alignment with the direction of the applied field. Domains in the material in which the magnetic moments are more or less aligned with the applied magnetic field increase in size at the expense of neighboring domains that are more or less oppositely aligned to the applied field. The consequence of such domain wall motion is that the material acquires a magnetic moment that may be considered as the resultant of all of its atomic moments. Therefore, the magnetic moment of the specimen provides a measure of the degree of alignment of the atomic moments [13].

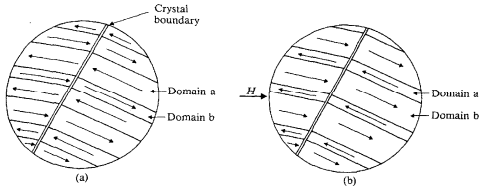

Fig. (1) Ferromagnetic domains. (a) No applied magnetic

2.3.3 Definition of Magnetic Saturation

The magnetization of ferromagnetic material is caused by the movement of magnetic domain walls and the rotation of magnetic domains. Figure (2) shows several states of magnetization. In the figure, the arrows represent the direction of spontaneous magnetization of each magnetic domain. The ideal demagnetized state is shown at point O.

A direction of spontaneous magnetization in each magnetic domain is distributed randomly. When a positive magnetic field is applied, domains magnetized in the minus direction are eliminated first, by 180° wall motion, leading to the distribution shown at B. Further increase in magnetic field rotates vectors into the state of saturation shown at C. Also, magnetic saturation of the material is defined in this state. When the field is now removed, the domain vectors fall back to the easy direction in each grain nearest to the +H direction. The domain vectors are uniformly spread over one half of a sphere, as indicated at D. In Fig. (2), we can see the states at O and D are different. If we apply a magnetic field in the other direction, the magnetization arrives at E and its state is also different from the state of the grain at O. When the rotor which has permanent magnets on its surface rotates for several cycles, this process is repeated.

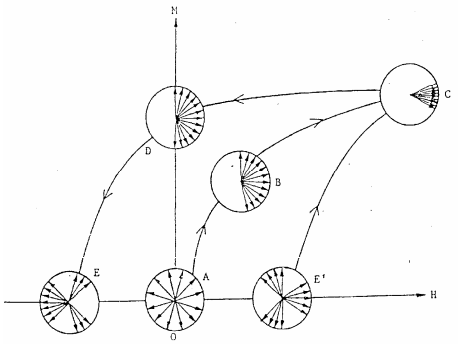

Fig. (2) Domain arrangement for various states of magnetization [14]

3. Overview of Permanent Magnet Synchronous Motor Test System

The requirements for the test bed performance are to generate nonlinear dynamic loads, to emulate the test state as in a real situation, and to observe and evaluate coupled nonlinear properties [22-25]. The test bed is designed for testing different kinds of motors and actuators but the results shown in this paper presents primarily the magnetic flux response for the Permanent Magnet Synchronous Motor (PMSM).

3.1 Hardware Implementation

A schematic diagram of the test bed is shown in Fig. (3). The diagram shows the signals flow from the sensor readings and the control reference signals are formed at the motion controller. The test bed was designed to accommodate actuators and electric motors up to 1 HP in capacity. Since different 1 HP systems can have a large variation in torque-speed relationships, the mechanical components of the test bed were designed and selected for both high-speed and high-torque operations. A 4000RPM, 10HP (peak 5000RPM and 48Nm torque) motor was selected as the load motor. Its primary purpose was to provide a programmable dynamic load. The test motor and the load motor were connected through a series of Bellow couplings that were selected for minimal inertia, maximum stiffness, high torque and high speed capacity. In between the mechanical couplings were other components such as a brake, clutch, torque sensor, etc. Each coupling can endure more than 54Nm in torsion. All components were held rigidly against a variety of load profiles by long steel rails. Set screws are used for the fine adjustment of the pitch and yaw of each component. Also, the specifications of the primary components in the test bed are shown in Table (1).

Several sensors, including three current sensors, two position encoders, four thermistors, one magnetic flux density sensor and one torque sensor were used to develop the performance data sets and to monitor the test motor state variables in real time. The current sensors measured three phase input currents to the test motor. A 12 bit incremental encoder was used to determine precise rotor position. A 1kHz bandwidth Surface Acoustic Wave (SAW) torque sensor was used to fully measure the performance of an actuator and to enable torque control of the load motor. The installation of a magnetic flux sensor will be described in detail in order to support the idea of measuring the magnetic saturation that occur in permanent magnets in Section 3.4. For detailed specifications of these sensors refer to Table (1).

Table 1. Primary Component Specifications

Key Components	Features
Load Motor	10HP (Peak), 48.3 Nm, 5000 RPM (No load speed), 81 Amps (Peak)
Test Motor	0.78HP (Max), 26 Nm (Peak), 600 RPM 17.2 Amps (Peak)
Torque Sensor	40 Nm (Max), 15000 RPM, +/- 0.5% (Accuracy)
Encoder	12 Bit (Resolution), 6000 RPM (Max)
Clutch	68 Nm (Max), 4000 RPM
Current Sensor	36 Amps (Peak). +/-0.5 (Accuracy)
Motion Controller	16 kHz (Sampling rate), 8 AIO (16 bit), 16 DIO

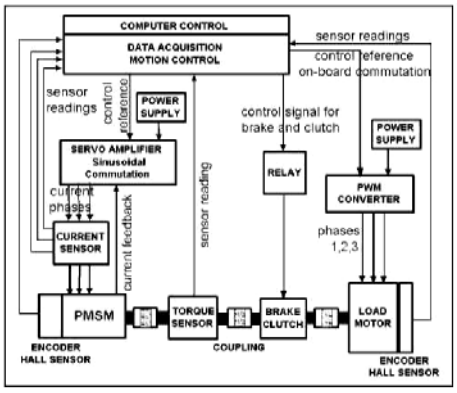

Fig. (3) Overview of the actuator test bed

3.2 Motion Controller

PMSMs are sinusoidally commutated. Commutation is implemented electrically with a drive amplifier that uses semiconductor switches to change current in the windings based on rotor position feedback [15]. There are two common methods to vary the current supplied to the motor windings. The traditional method depends on the amplifier to commutate the current (based on feedback) supplied to the motor. The second method is to use a motion controller to commutate the first two phases and to allow an amplifier to determine the value of the third phase [16]. Since the sum of the currents at any time is zero, the current in the third phase equals the inverse of the first two currents. A National Instruments (NI) motion controller was used to provide sinusoidal commutation to the load motor.

NI products were critical to the instrumentation, control, and software development of this test bed. For motion control, NI's PXI-7350 8-axis motion control card was used. Two axes of this board were used for the load motor and one for the test motor. The load motor drive did not need encoder and Hall sensor feedback because the motion controller did the sinusoidal commutation of the load motor. As such, the Hall and position feedback signals were directly sent to the PXI-7350. For the test motor, encoder and hall signals were needed for feedback to the amplifier and completed the sinusoidal commutation loop to run the test motor. Also, in order to control the test motor in torque mode, the torque sensor analog signal was connected to one of the analog input channels on the NI motion controller. This channel was then used as a feedback signal for the test motor. With this arrangement, the load motor was speed controlled while the test motor was torque controlled.

The brake and clutch were instrumental to maintain safe operation of the test bed. The motion controller sent the operational commands for the clutch. Default setting for the clutch was "off". This was done to prevent the unintentional transfer of large torques from the load motor to the test motor during initialization.

3.3 Data Acquisition

The values of interest from sensors in the test bed were position, velocity, acceleration, torque, temperature, magnetic flux, voltage, and current. An NI-SCXI signal pre-conditioning module cleaned up the noisy raw data from the test bed. The SCXI 8^{th} order programmable Bessel filter was installed in the test system. The SCXI-1142 Bessel lowpass filter provides 80dB attenuation and the passband magnitude response begins to drop off immediately with 7kHz cutoff frequency. A Bessel filter has almost zero phase shift and it is not sensitive to overshoot or ringing in the step response. For data acquisition, an NI-PXI-6040E multifunctional DAQ board was used to read the 12 analog input signals at 22.7kHz per channel, 12-bit resolution. The Real Time System Integration (RTSI) bus connected internally in the PXI machine was used for high speed data synchronization. NI-Motion and Measurement & Automation Explorer (MAX) configuration utility was used to provide complete control over the characteristics of the actuator control system.

3.4 Installation of Magnetic Flux Density Sensor

The Hall generator is used to measure magnetic flux density which is a solid-state type of sensor. This sensor provides an output voltage proportional to magnetic flux density. The Hall effect develops a voltage across a conductor when current is flowing and the conductor is placed in a magnetic field. The voltage is potentially generated across the width of the conductor is called the Hall voltage. The Hall voltage can be given as follows.

$$V_H = \gamma_B B \sin\theta \qquad (6)$$

where V_H is Hall voltage (mV), γ_B is the magnetic sensitivity (mV/kG), B is the magnetic field flux density (kG), and θ is the angle between magnetic flux vector and the plane of Hall generator. The sensor used in this research needed current source (100mA) and its sensitivity was set as 8.60mV/kG.

The air gap between the rotor and stator poles of the motor was 0.03" and the thickness of the Hall sensor was 0.02". Therefore, the sensor was barely able to be installed in the air gap without causing any mechanical problem.

4. Temperature Effects on Magnetic Material

4.1 Magnetic Exciting Current Curve

The waveform of the magnetic field in the core requires an exciting current in the exciting stator windings. The nonlinear relationship between magnetic flux and current in Figure 8 means that the waveform of the exciting current differs from the sinusoidal waveform of the flux. A curve of the exciting current as a function of time can be found graphically from the desired magnetic characteristics as illustrated in Fig. (4).

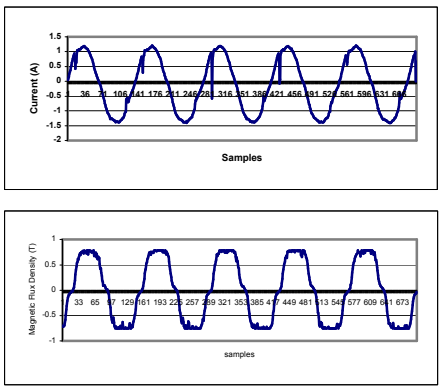

Fig. (4) Current and magnetic flux density data in 150RPM, 0.75A (RMS)

Since magnetic flux density, B, and magnetic field intensity, H, are related to magnetic flux, ϕ, and current, i_ϕ, by known geometric constants, the hysteresis loop can be drawn using ϕ=BA and iϕ=Hl/N as shown in Fig. (5). At very low frequencies, the magnetic flux linkage and current loop can be obtained from the similar shape of the B-H loop (see Fig. 5). At higher frequencies, the B-H loop is broadened due to

the effect of eddy currents. Slemon explains this phenomenon more carefully in his book [12].

When the exciting current has more than one cycle and a constant RMS value, there is almost no variation of B with H. The magnetic material starts to be magnetized by the variation of magnetic flux density from the unmagnetized point as shown in Fig. (6). If we look at Fig. (6) more carefully, the arrow-head indicates the direction of movement of the point representing the magnetic state of the magnetized material as H alternates slowly [12]. At point 'A' in Fig. (5), the magnetic flux is not increasing any more. It is said to be "Saturated." Then, as the strength of the magnetic field is reduced, the material does not go back to its former state because this process is irreversible.

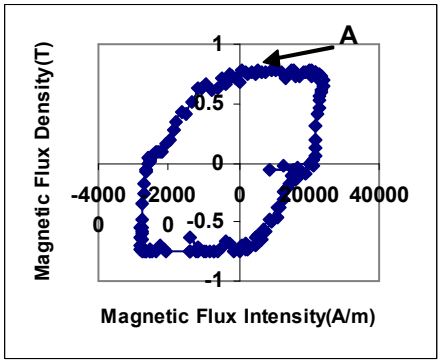

Fig. (5) B-H curve of PMSM

When the magnetic flux strength, which is the same as the magnetic field intensity, is zero, the value of the magnetic flux density is called by the residual magnetic flux density. From this point, the curve will follow the demagnetization process as illustrated in the second quadrant. When the magnetic flux density is zero, it is defined by a coercivity force. Now, it follows to the negative direction of the pole. The complete loop is known as a Hysteresis loop. Rotating the rotor of the PM motor creates this Hysteresis loop at the same speed.

4.2 Change of Magnetic Saturation

As mentioned before, the magnetic moments of materials are held in parallel or anti-parallel by exchanging forces. This is due to the sharing or exchange of electrons between neighboring atoms in the crystal structure of the material. When the temperature of a material is increased, each atom oscillates about its mean position in the crystal lattice, and this oscillation disturbs the alignment of the spin magnetic moments [12,14]. Consequently, as the temperature of a ferromagnetic material is increased, its magnetization decreases as shown in Fig. (7).

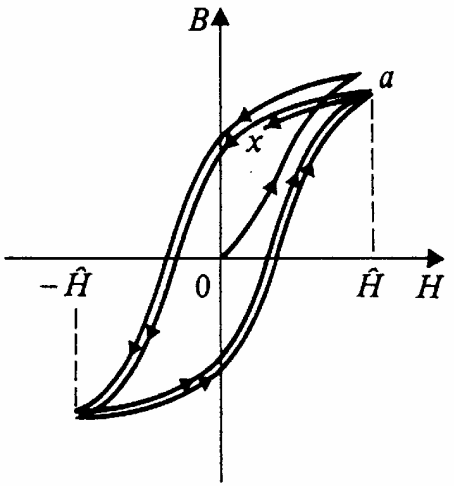

Fig. (6) Variation of B with H [12]

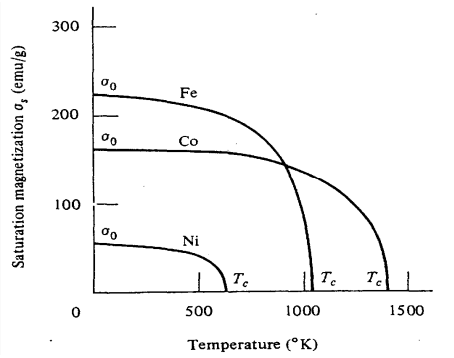

Fig. (7) Saturation of Fe, Co, and Ni as a function of temperature [12]

At a temperature known as the Curie temperature, T_C, the parallel alignment completely disappears and the magnetic moments become randomly aligned. The definition is given in the AIP handbook [17], "Curie point, as the temperature increases, at which the transition from ferromagnetic to paramagnetic properties of a substance is complete." For this paper, an iron magnetic core has been assumed. The Curie temperature for iron is 770°C [14]. Since the temperature in most electric machines is usually below 150°C, the effect of the temperature on the ferromagnetic property of iron is small. Nd-Fe-B, rare earth material, is used for a permanent magnetic material. It has a very low Curie temperature, 320°C, compared with the other pure materials in a motor [13].

However, the bend point of the saturation magnetization curve in Fig. (7) is of interest in this research. The magnitude of magnetic flux of a magnet starts to reduce from this bend point when it loses its magnetization at a high temperature. The Nd-Fe-B permanent magnet material has a property of a negative high slope of its magnetic flux value with temperature as shown in Fig. (8). Therefore, it is hard to decide the exact bend point because the tendency of

magnetization is different from the case of a pure material.

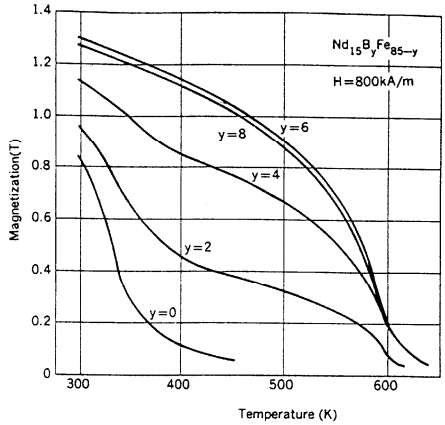

Fig. (8) Magnetization curves of Nd-Fe-B magnets containing different percentages of boron [18]

When the temperature, 65°C (338K), is applied to Fig. (8), then the corresponding magnetic flux density, B, is 1.24T and the magnetic susceptibility, χ, is 1 and the value of Boron component is 8. The reduction of magnetic flux density from 1.3T to 1.24T means the magnetic material reaches its saturation state faster by increased temperature of operation of the PM motor. Moreover, the magnetic flux density curve decreases linearly between 300K and 423K in Fig. (8). This means that magnetic flux density and temperature have a linear negative relationship. Therefore, based on this information, magnetic flux density is 1.1T at 150°C (423K) which is a 15% reduction.

5. Analysis

5.1 Temperature Effects on the Production of Magnetic Flux Density

Tomy Sebastian mentions in [19] that temperature affects PM motors using Nd-Fe-B magnets on their torque production capability and on the efficiency of the motor. If a careful design of PM motor is performed, the irreversible demagnetization is avoidable at elevated temperatures. One of the ways to improve the design of the PM motor is to equip it with a better cooling system. When PM motors are designed to operate in a wide temperature range, the reversible demagnetization of the Nd-Fe-B magnets with temperature and the increase in winding resistance with temperature influence the resulting maximum torque capability at rated speed and efficiency of the PM motor. Figure (9) is the experimental result and represents the changes of magnetic flux density with sinusoidal current inputs in three phases. The flux density was saturated at 0.8T at 25°C (Solid line in Fig. 9), and it is reduced to a smaller value at 78°C (Dotted line in Fig. 9). Thus, the torque produced from this motor will be affected by the reduction of the magnetic flux density at higher temperatures because the torque is a function of flux and current as shown in Eq. (4). This result helps to understand the temperature affects on the performance of the PM motor. In this test, the magnetic flux density always has the same maximum saturated value in any speed and reference current input because the flux measured in the sensor estimates the magnetic strength of the PM bonded on the rotor.

5.2 Torque Saturation Limit

As mentioned above, the PM motors using temperature sensitive magnetic cores with a relatively low Curie temperature have different speed and torque characteristics as compared with conventional motors when considering temperature changes. As the temperature increases to a critical point, (which is out of range of operating temperature), the residual flux density and intrinsic coercivity of Nd-Fe-B magnet will go down because the end point of the B-H curve cannot reach the magnetic saturation value at the critical temperature as shown in Fig. (9). Output torque in the PM motor is saturated at this time and the torque saturation limit is obtained at the critical magnetic flux density and the critical temperature.

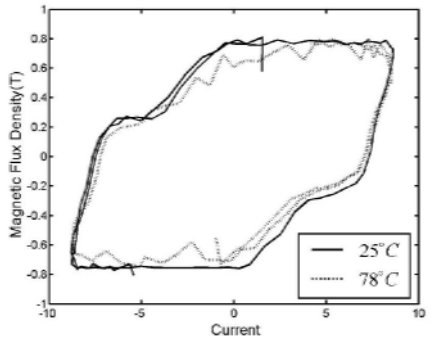

Fig. (9) Magnetic flux density and current curve in two different temperatures (Solid line: 25°C, Dotted line: 78°C)

The saturated magnetic flux density varies with the change in armature resistance and flux reluctance of the motor with an increased temperature. It follows that the magnetic flux is directly related with the magnet residual flux density. Figure (9) illustrates this phenomenon for Nd-Fe-B. If the motor operates for a long time and results in generating large amounts of energy, it is transformed to heat and the temperature goes up. Therefore, energy losses also increase. In the B-H curve of Fig. (6), the end point of the arrow is the trajectory of the curve of magnetic flux and current. Therefore, when torque saturation occurs, the end point of the arrow indicates a lower value than the magnetic saturation point. The reason why the

end tip of the B-H curve indicates a lower point is that the fully saturated magnetization of the magnetic material of the rotor changes to a less saturated state. This point comes from Fig. (8), which illustrates the relationship between saturated magnetization and Curie temperature.

If the starting point of the B-H curve is known in Fig. (5) and (6), the end point of the arrow makes a slightly different trajectory and the time, cycle, current and magnetic flux are recorded during the whole operating time. Both magnetic flux density, B, and current density, J, have a current property. They also have rms values because Slemon's PM motor has alternating waveform signals. The accumulation of the values of the magnetic flux density and current obtained as a function of cycle or time stops at the value of cycle or time that indicate a specific lower value of magnetic saturation point. Figure (10) explains these procedures graphically. When a higher temperature makes faster magnetization of the permanent magnets, the lower flux density value (1.1T in the previous example) indicates a torque saturation limit. Now, we can define the torque saturation limit by using Eq. (4), which is the torque equation of the model used in this paper, as

$$T_{sat} = r\,A\,B_{rms}\big|_{\theta_1}\,J_{rms}\big|_{\theta_1} \quad \text{N.m} \qquad (9)$$

where r is the radius, A is the area of normal flux direction, B_{rms} is the rms value of magnetic flux density, J_{rms} is the rms value of current density, and θ_1 is the cycle which indicates a specific lower value of magnetic saturation limit.

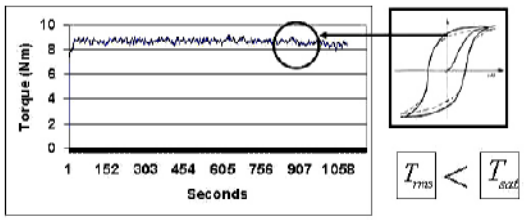

Fig. (10) Forecasting the torque saturation by monitoring magnetic flux–current curve

Given a torque saturation limit, T_{sat}, the duty cycle norm is defined with a root-mean-square (rms) value of torque output on the motor, which takes into account the fluctuations of the signal about its average value. The operation of computing the average value of torque output corresponds to integrating the signal waveform over some period of cycle. The cycle averaged value of a torque or duty cycle norm is defined as

$$T_{rms} = \sqrt{\frac{1}{t_{cycle}}\int_0^{t_{cycle}} T^2 d\theta} \qquad (10)$$

where t_{cycle} is the period of a cycle, θ is a cycle, and T is the torque measurement

6. Conclusions

This paper showed the hysteresis loop of magnetic flux and current by testing a real electric motor, but did not demonstrate the value of torque saturation limit reached at an elevated temperature (such as 150°C). Due to the limitation of operational temperature in a test motor, the motor was not operated over 80°C in order to not damage the test motor. For the best test set-up to get the torque saturation limit, the permanent magnet material used in the test motor should be tested individually at the elevated temperature. In conclusion, if the torque saturation limit is considered to evaluate a motor, a more careful design about each parameter is necessary and an experiment must be performed to find the exact value of the torque saturation limit.

References

[1] P. Pillay, *IEEE Trans. on Indust. Appl.*, 25(2) (1989) 265-273.
[2] T.W.J. Sokira, **"Brushless DC Motors Electronic Commutation and Controls"**, TAB (NY 1990).
[3] N. Hemati, *IEEE Trans. on Indust. Appl.*, 28(1) (1992) 172-180.
[4] D.A. Stone, T.S. Birch, and K.N. Leonard, "A versatile computer controlled dynamometer test system", *Symp. on Power Electronics, Electrical Drives, Advanced Electrical Motors* (June 1994) 353-358.
[5] K.A. Corzine et al., *IEEE Trans. on Energy Conv.*, 13(3) (1998) 270-275.
[6] A.E. Fitzgerald, Jr., S.D. Umans, **"Electric Machinery"**, 5 ed. McGraw Hill (London 1992).
[7] H. Hofmann, S. Sanders and C.R. Sullivan, *IEEE Trans. on Indust. Appl.*, 33(4) (1997) 935-942.
[8] H. Le-Huy, and R. Feuillet, *IEEE Trans. on Indust. Appl.*, IA-22(4) (1986) 790-797.
[9] P.R.K. Pillay, *IEEE Trans. on Indust. Appl.*, 27(5) (1991) 986-996.
[10] R. Rabinovici, *IEE Proc. of Electric. Power Appl.*, 141(1) (1994) 7-11.
[11] F. Deng, *IEEE Trans. on Energy Conv.*, 14(4) (1999) 1391-1395.
[12] G.R. Slemon, **"Electric Machines"**, Addison-Wesley Publishing Company (MA 1980).
[13] R.J. Parker, **"Advances in Permanent Magnetism"**, John Wiley &Sons (NY, 1990).
[14] B.D. Cullity, **"Introduction to Magnetic Materials"**, Addison-Wesley Publishing Company. Inc (CA 1972).
[15] Advanced Motion Controls, PWM Servo Amplifiers – Catalog and Technical Manual, Camarillo, CA, 1999-2000
[16] National Instruments, Measurement and Automation Catalog, Austin, TX, 2003

[17] D. Gray, "**American Institute of Physics Handbook**", 3 ed. (NY 1972).
[18] M. Sagawa et al., *J. of Appl. Phys.*, 55(6) (1984) 2083-2087.
[19] T. Sebastian, T., *IEEE Trans. on Indust. Appl.*, (1995) 353-357.
[20] R.W. Newton, R.E. Betz and H.B. Penfold, "A dynamic dynamometer for testing variable speed drives", *IEEE Industry Applications Society Annual Meeting Conference*, 1 (October 1994) 538-544.
[21] D.C. Youla and J.J. Bongiorno, *IEEE Trans. on Circuits and Systems*, CAS-27 (1980) 15-19.
[22] E.R. Collins and Y. Huang, *IEEE Trans. on Energy Conv.*, 9(3) (1994) 521-527.
[23] Test Procedures for Synchronous Machines, "Part I – Acceptance and performance testing; Part II – Test procedures and parameter determination for dynamic analysis," IEEE 115, 1995.
[24] A. Wallace, A. von Jouanne and T. Rollman, "A fully regenerative, high power testing facility for motors, drive & generators", *IEEE International Electric Machines and Drives Conf. Record*, (1997) MB2/13.1 -MB2/13.3.
[25] J. Hsu et al., *IEEE Trans. on Indust. Appl.*, 34(1) (1998).

CALL FOR PAPERS
43rd Annual Asilomar Conference on Signals, Systems, and Computers

Asilomar Hotel and Conference Grounds
Pacific Grove, California
November 1-4, 2009
www.asilomarssc.org

Authors are invited to submit papers before June 1st, 2009, in the following areas:

A. Communications Systems: 1. Error Control Coding, 2. CDMA, 3. Modulation and Detection, 4. Performance Bounds, 5. Synchronization, 6. Ultra Wideband, 7. OFDM / Multicarrier, 8. Wireless Communications, 9. Optical Communications, 10. Cognitive SDR, 11. Adaptive Waveform Design

B. MIMO Communications and Signal Processing: 1. Space-Time Coding and Decoding, 2. Channel Estimation and Equalization, 3. Multi-User and Multi-Access Methods, 4. Cooperative Diversity.

C. Networks: 1. Transmission Techniques for Ad Hoc Networks, 2. Wireless Sensor Networks, 3. Network Information Theory, 4. Optical Networks

D. Adaptive Systems and Processing: 1. Adaptive Filtering, 2. Fast Algorithms for Adaptive Filtering, 3. Frequency -Domain and Subband Adaptive Filtering

E. Array Processing and Statistical Signal Processing: 1. Array Processing and Beamforming, 2. Sonar and Acoustical Array Processing, 3. Radar Array Processing, 4. Remote Sensing, 5. Signal Separation, 6. Estimation and Detection, 7. Non-Gaussian and Nonlinear Methods, 8. Identification, 9. Compressive Sensing, 10. Information Theoretic Signal Processing, 11. Spectral Analysis

F. Biomedical Signal and Image Processing: 1. Medical Image Analysis, 2. Imaging Modalities, 3. Advances in Medical Imaging, 4. Biomedical Signal Processing, 5. Biomedical Applications, 6. Bioinformatics, 7. Image Registration and Multi-modal Imaging, 8. Image Reconstruction, 9. Computer Aided Diagnosis, 10. Functional Imaging, 11. Visualization

G. Architecture and Implementation: 1. Programmable and Reconfigurable Architectures, 2. SOC Architectures, 3. Low-power Methods, 4. Compilers and Tools, 5. Integrated Algorithm and Architecture Implementation, 6. Computer Arithmetic, 7. Numerical Processing

H. Speech, Image and Video Processing: 1. Speech Processing, 2. Speech Coding, 3. Speech Recognition, 4. Narrowband / Wideband Speech and Audio Coding, 5. Document Processing, 6. Models for Signal and Image Processing, 7. Image and Video Coding, 8. Image and Video Segmentation, 9. Image and Video Analysis, 10. Image / Video Security, Retrieval and Watermarking, 11. Image and Video Enhancement / Filtering, 12. Biometrics and Security, 13. Wavelets

Submissions should include a 50 to 100 word abstract and an extended summary (500 to 1000 words, plus figures). Submissions must include the title of the paper, each author's name and affiliation, and the technical area(s) in which the paper falls with number(s) from the above list. Check the conference website (www.asilomarssc.org) for specific information on the electronic submission process. Submissions will be accepted starting February 1, 2009. **No more than FOUR submissions are allowed** per contributor, as author or co-author. **All submissions must be received by June 1, 2009**. Notifications of acceptance will be mailed by mid August 2009, and author information will be available on the conference website by late August 2009. Full papers will be due shortly after the conference and published in early 2010. All technical questions should be directed to the Technical Program Chair, **Dr. Jim Schroeder**, e-mail jim.schroeder@harris.com, or the General Chair, **Dr. Maïté Brandt-Pearce**, e-mail: mb-p@virginia.edu. Prospective organizers are invited to submit proposals for **special sessions** to jim.schroeder@harris.com or mb-p@virginia.edu by January 15, 2009. Proposals must include a topical title, rationale, session outline, contact information, and a description of how the session will be organized.

CONFERENCE COMMITTEE

General Chair:	Maïté Brandt-Pearce, *University of Virginia*
Technical Program Chair:	Jim Schroeder, *Harris Corporation*
Conference Coordinator:	Monique P. Fargues, *Naval Postgraduate School*
Publication Chair:	Michael Matthews, ATK *Mission Research*
Publicity Chair:	Murali Tummala, *Naval Postgraduate School*
Finance Chair:	Frank Kragh, *Naval Postgraduate School*

The site for the 2009 Conference is at the Asilomar Conference Grounds, in Pacific Grove, CA. The grounds border the Pacific Ocean and are close to Monterey, Carmel, and the scenic Seventeen Mile Drive in Pebble Beach.

The Conference is organized in cooperation with the Naval Postgraduate School, Monterey, CA, and ATK Mission Research, Monterey, CA. The IEEE Signal Processing Society is a technical co-sponsor of the conference.

Selma M.H. Al-Jawad

School of Applied Sciences, University of Technology, Baghdad, IRAQ

Effect of pH value on the Photoconductivity of Chemically Deposited CdS Thin Films

Highly photosensitive CdS thin films with photocurrent to dark current ratio (I_{ph}/I_d) of ~10^5 under 300W.m^{-2} illumination were reported. The films are prepared by an electroless chemical deposition technique. The pH value of the solution used in the electroless deposition of cadmium sulfide thin films has been found to affect the deposition rate, optical transmission, photoconductivity, photoconductivity to dark conductivity ratio σ_{ph}/σ_d and photocurrent decay time.

Keywords: CBD, Polycrystalline CdS films, Optoelectronic characteristics

Received: 12 July 2008, **Revised** 20 August 2008, **Accepted**: 27 August 2008

1. Introduction

Current interest in direct energy conversion devices has led to renewed research in the area of materials for such devices [1-3]. Cadmium sulfide thin films can be prepared by different methods such as vapor deposition, sputtering,

need for a simple yet reliable technique for producing large area cells of CdS of high stoichiometry, this report on the preparation of chemically bath deposited films would appear to be topical. Various factors affecting the deposition process have been studied in order to understand the process of deposition and thus to improve the characteristics of the films.

The basic mechanism of the film formation in this technique is an ion-by-ion condensation of Cd^{2+} and S^{2-} ions on the substrate from an aqueous basic medium, pH>10, containing thiourea and cadmium ions. The cadmium ions are present in the form of a complex species in solution, the dissociation of which causes the slow release of Cd^{2+} ions for the formation of the thin film [4]. In the case where thiourea is employed in an alkaline medium, the sulfide ions are released as follows [5]:

$$Sc(NH_2)_2 + OH^- = CH_2N_2 + H_2O + SH^- \quad (1)$$

$$SH^- + OH^- = S^{2-} + H_2O \quad (2)$$

Using $CdSO_4$ with ammonia (NH_4OH) will form cadmium complex $[Cd(NH_3)_4]^{2+}$ according to the following equation [6]:

$$CdSO_4 + 2NH_3 = [Cd(NH_3)_4]SO_4 \quad (3)$$

Then CdS will form according to the following equation:

$$[Cd(NH_3)_4]_{2+} + S^{2-} = CdS + 4NH_3\uparrow \quad (4)$$

Our major interest in this work was the development of CdS thin films of high chemical spray deposition and chemical bath deposition. CdS has been widely accepted as one of the most sensitive photoconductors and its status as promising thin film solar cells material is sustaining continued interest in this material [4]. In the context of the photoconductivity to serve as window material in heterojunction solar cells [7,8].

2. Experiment

2.1 Chemical deposition of the films

Substrates of borosilicate glass slides were used for deposition. They were first cleaned in distilled water in order to remove the impurities and residuals from their surfaces then rinsed in chromic acid for 24 hours to introduce functional groups called nucleation and/or epitaxial centers, which form the basis of the thin films growth [9]. Then the samples were washed repeatedly in deionized water and finally put in ultrasonic agitation with distilled water for 15min then dried.

The deposition of CdS films is achieved from dilute solutions. Sulfide ions are released in the bath by the hydrolysis of thiourea, in the presence of OH^- ions. Cd^{2+} ions are complexed with one or more of the complex agents like NH_3 [directly added as NH_3(aq)], or NH_4Cl. This ensures slow release of Cd^{2+} ions in the solution [10]. Films were deposited on glass slides using slowly-mixed 0.1M ($3CdSO_4.8H_2O$), NH_3 solved in distilled water at room temperature with continuous stirring. Substrates were then immersed in a beaker containing the reaction mixture. The beaker was placed in a water bath at temperature of (80±2°C). It was heated with continuous stirring to the required temperature of

 ISSN 1813-2065

deposition. The solution was stirred with a magnetic stirrer type (MSH-300). Then 30ml of 0.2M thiourea solution was added with continuous stirring. The pH was measured with pH-meter type (BIBBY 211). After 20 minutes, substrates were then taken out and washed with distilled water and ultrasonic agitation to remove the porous cadmium sulfide over layer, then dried.

2.2 Measurements

In order to measure the electrical properties of 2cm^2 samples, ohmic contacts were made by vacuum evaporation of high-purity (99.999) indium wire. Evaporation process was started at a pressure of 10^{-5}torr and the best condition for good ohmic contact was satisfied by a layer of 200nm, which was determined by weighing method.

In illumination measurements, a halogen lamp connected to a variac and calibrated by power meter, was used. The bias and current measurements were performed using Keithley-602 electrometer and d.c. voltage source. The bias was 10V in all cases. The photocurrent response was measured for total duration of 1600s for each sample as follows: the first 200s in dark, the subsequent 400s under 300W.m^{-2} simulated solar radiation and the last 1000s with the illumination shutoff to facilitate the dark decay of the photocurrent. All measurements were done at room temperature (24°C).

A Cecile CE-7200 spectrophotometer supplied by Aquarius company was used to introduce the optical transmission for CdS thin films deposited on glass substrates in the wavelengths range (375-900) nm.

3. Results and Discussion

3.1 The optical transmission

The spectra shown in Fig. (1) represent the transmittance of the films deposited at different pH values. It was found that the transmittance of the deposited films is high at long wavelengths (70-80%) and decreases to 10% at short wavelengths. This is mainly because of the increased abundance and/or size of the single crystallite overgrowth. The increase and decrease in the transmittance during the continuous increase of [pH] is attributed to the transition of CdS phase from mixed cubic and hexagonal to hexagonal structure. With this result, pH of 11.5 is thought to be the optimum value to deposit CdS films used for photovoltaic applications.

3.2. The dark conductivity

The photocurrent response of the films deposited at different pH values are shown in Fig. (2). Some small random variation in the dark current level was observed. However, the stable dark current levels in all cases in Fig. (2) were found at about 10^{-11}A at 10V bias. The variations in deposition time do not cause any significant change in the conductivity and this emphasizes the preference for stoichiometry of the chemically deposited CdS thin films. This aspect was earlier studied by Danaher et al. [11], whose x-ray photoelectron spectroscopy studies yielded a normalized Cd:S ratio of 1.04±0.08 in the chemically deposited CdS films.

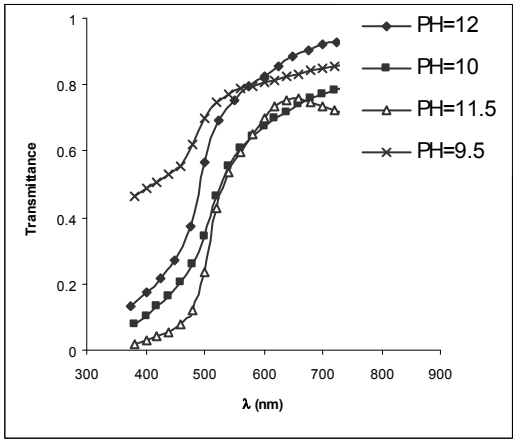

Fig. (1) The optical transmission spectra of CdS films for different pH value

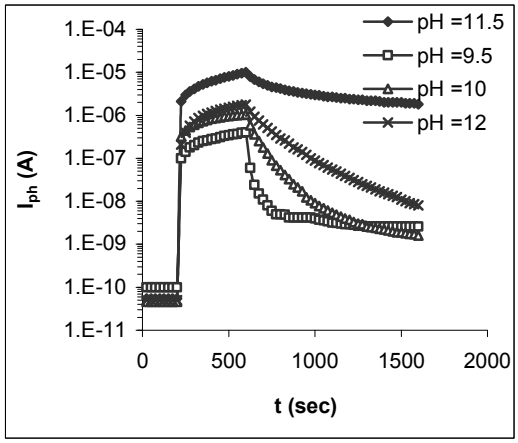

Fig. (2) Photocurrent response of the CdS films deposited for different pH value

3.3 The photoconductivity

The effect pH value on the photoconductivity of the chemically deposited CdS thin films are very significant, as seen in Fig. (2). The variation in the photoconductivity with pH values is explicitly shown in Fig. (3).

It is generally accepted that the photoconductivity in CdS thin films follows the models of Orton et al. [12]. On the basis of these models, the photoconduction in CdS films is mainly ascribed to photogenerated electrons. The photogenerated holes make a rather indirect contribution by enhancing the electron mobility when the trapping of photogenerated holes at the

inter-grain barriers reduces the barrier height, thereby promoting the electron transport [14].

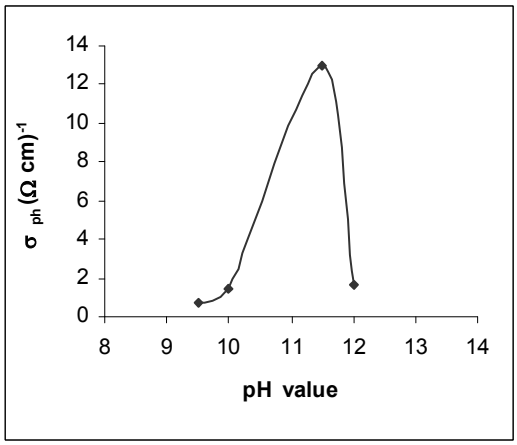

Fig. (3) Photoconductivity of the CdS films recorded at the end of 10 min of illumination (300 W m^{-2} simulated solar radiation) for different pH value

The variation in the photoconductivity in different films under the same illumination condition, as in the present work, can arise from the variation in either the electron mobility (μ_n) or the free lifetime (τ_n) of the photogenerated electrons in the equation [13]

$$\sigma_{ph} = eG\mu_n\tau_n \qquad (5)$$

where σ_{ph} is the photoconductivity, e is the electron charge and G is the photo-carrier generation rate, which in the present case (300W.m^{-2}) is estimated to be about 10^{20} electron-hole pairs.cm^{-3}.s^{-1}. The maximum photoconductivity of 1.32(Ω.cm)$^{-1}$ (at 90^{o}C) observed in this work yields the mobility-lifetime product for electrons as $\mu_n\tau_n$~0.1cm^{-1}V^{-1}.

Since the measurement of the mobility was not performed, it was not possible to ascertain if the increase in the mobility-lifetime product with the decreasing bath temperature is due to the increase in mobility or due to an increase in the carrier lifetime. In polycrystalline CdS films, there is an increase in electron mobility due to increase in grain size [14]. The higher mobility-lifetime product increases the diffusion length (L) and leads to an increased short-circuit current. Also, since the series resistance of the cell is inversely proportional to the carrier mobility, as well as to the carrier concentration, higher carrier mobilities are desirable in such applications. The variations in mobility-lifetime with pH values are shown in Fig. (4).

3.4 The photocurrent decay time

Figure (5) shows the variations in the photocurrent decay time with pH value. The decay time refers to the time required for the photocurrent value attained at the end of exposure (400S, 300W.m^{-2} illumination) to decay to 1/e of this value.

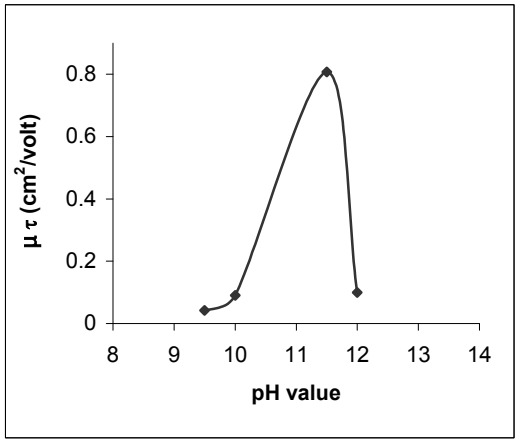

Fig. (4) The variation in mobility-lifetime with pH value

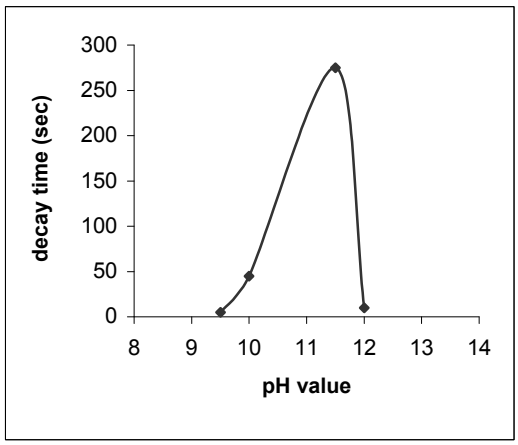

Fig. (5) Effect of the pH value on the photocurrent (300W.m^{-2} simulated solar illumination) decay time

3.5 The photocurrent-to-dark current ratio

Figure (6) shows the photoconductivity-to-dark conductivity ratio (σ_{ph}/σ_d) for the deposited films as a function of pH value. Values of the above ratio are among the highest reported for CdS films.

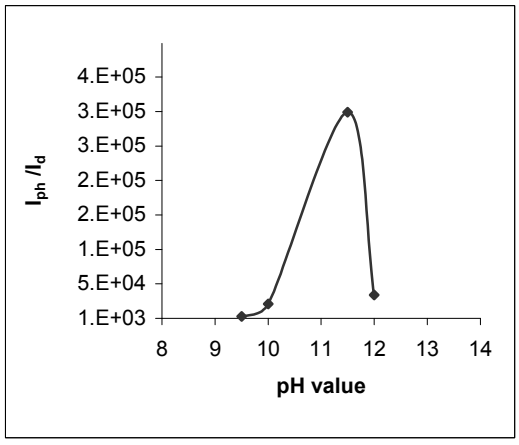

Fig. (6) Photocurrent to dark current ratio of the CdS films with pH value

The best value reported for the chemically deposited CdS films prior to our results appears

to be 10^6 by Danaher et al. Even though a high value of σ_{ph}/σ_d is not a crucial factor for solar cell applications, it is a primary requirement for photodetector applications. CdS is one of the two most sensitive photoconductors and hence it has established its place in numerous photodetecting devices [13,15].

4. Conclusions

In this paper, it was reported that the pH value of the solution has significant influences on the photoconductivity characteristics of chemically deposited CdS thin films. High quality of CdS thin films was obtained by the chemical deposition technique. It was reported that CdS films of conductivity greater than $13(\Omega.cm)^{-1}$, required for heterojunction solar cells, can be achieved without any doping. This improvement was made possible merely by varying the chemical bath parameters, so that it contains the cadmium salt and thiourea in the molar ratio 1:1.

References

[1] N.R. Pavaskar, C.A. Menezes and A.P.B. Sinha, *J. Electrochem. Soc.*, 124(5) (1977) 743-748.
[2] K.S. Ramaiah et al., *Mater. Chem. and Phys.*, 68 (1977) 22-30.
[3] T. Pisarkiewicz, E. Schabowska and E. Kusior, *J. Wide Bandgap Mater.*, 9(9) (2001) 127-132.
[4] P.K. Nair et al., *Solar Cells*, 22 (1987) 211-227.
[5] P.K. Nair and M.T.S. Nair, *Solar Cells*, 22 (1987) 103-112.
[6] S.N. Sahu and S. Chandra, *Solar Cells*, 22 (1987) 163-173.
[7] H. Metin and R. Esen, Photoconductivity studies on CdS films grown by chemical bath deposition technique, Erciyes Universitesi Fen Bilimleri Enstitusu Dergisi, 19(1-2) (2003) 96-102.
[8] I.O. Oladeji et al., *Thin Solid Films*, 359 (2000) 154-159.
[9] F.I. Ezema and P.E. Ugwuoke, *The Pacific J. Sci. & Technol.*, 5(1) (2003) 33-38.
[10] R. Grecu et al., *J. Optoelectron. Adv. Mater.*, 6(1) (2004) 127-132.
[11] W.J. Danaher, L.E. Lyons and G.C. Morris, *Solar Ener. Mater.*, 12 (1985) 137-148.
[12] J.W. Orton et al., *J. Appl. Phys.*, 53(3) (1982) 1602-1616.
[13] M.T.S. Nair, P.K. Nair and J. Campos, *Thin Solid Films*, 161(1-2) (1988) 21-34.
[14] A. Mondal, T.K. Chaudhuri and P. Pramanik, *Solar Ener. Mater.*, 7 (1983) 431-438.
[15] D. Patidar et al., *Bull. Mater. Sci.*, 29(1) (2006) 21-24.

The 4th International Conference on Information Theoretic Security 2009 (ICITS 2009)

Shizuoka, Japan 3-6 December 2009

Over the last few decades, we have seen several research topics studied requiring information theoretical security, also called unconditional security, where there is no unproven computational assumption on the adversary. (This is the framework proposed by Claude Shannon in his seminal paper.) Also, coding as well as other aspects of information theory have been used in the design of cryptographic schemes. Examples are authentication, secure communication, key exchange, multi-party computation and information hiding to name a few. A related area is quantum cryptography that predominantly uses information theory for modeling and evaluation of security. Needless to say, information theoretically secure cryptosystems are secure even if the factoring assumption or the discrete log assumption are broken. Seeing the multitude of topics in modern cryptography requiring information theoretical security or using information theory, it is time to have a regular conference on this topic.
This is the 4th conference of this series that is aimed to bring together the leading researchers in the area of information and/or quantum theoretic security. Original research papers on all technical aspects of information and/or quantum theoretic security are solicited for submission to ICITS 2009.

The topics of interest are (but not limited to)
Information Theoretic Analysis of Security, Public Key Cryptosystems using Codes, Conventional Cryptography using Codes, Authentication Codes, Key Distribution, Quantum Cryptography, Quantum Information Theory, Randomness Extraction, Secret Sharing, Secure Multiparty Computation, Oblivious Transfer, Anonymity, Ideal Ciphers, Traitor Tracing, Fingerprinting, Data Hiding and Watermarking, Information Hiding, Private and Reliable Networks

History
The 1st ICITS was held in October 16-19, 2005 in Japan under the name of 2005 IEEE Information Theory Workshop on Theory and Practice (ITW 2005), where the general co-chairs were Hideki Imai and Yuliang Zheng, and the program chair was Ueli Maurer. The 2nd ICITS was held in Madrid after Eurocrypt 2007, where the program chair was Yvo Desmedt. The 3rd ICITS was held in Calgary before CRYPTO 2008, where the program chair was Rei Safavi-Naini. These three conferences were great success.
Important Dates are

Submission deadline	Decision notification	Proceedings version	Conference
August 13 2009	September 15 2009	September 25 2009	December 3-6, 2009

Instructions for Authors
Submissions must not substantially duplicate work that any of the authors has published elsewhere or has submitted in parallel to a journal or any other conference/workshop that has proceedings.
The submission must be anonymous, with no author names, affiliations, or obvious references.
We strongly encourage to use Springer's LNCS format for submissions. The final proceedings version will be a paper of at most 18 pages in the llncs style, which corresponds to around 7000 words of text. The document submitted (excluding appendices) should correspond to what the author expects to be published if their paper is accepted without modification. We therefore strongly recommend that authors check whether their paper (without appendices) will fit within the above llncs space constraints.
The submission should begin with a title, a short abstract, and a list of keywords. The introduction should summarize the contributions of the paper at a level appropriate for a non-specialist reader. Committee members are not required to read appendices; the paper should be intelligible without them.
Submissions should preferably be in PDF format (pdf file) although PostScript (ps file) will be allowed. (The submission server will be available in late July, 2009.)

Proceedings:
Proceedings is planned to be published in Springer's *Lecture Notes in Computer Science*, and be available at the conference.
General Chair: **Akira Otsuka**
National Institute of Advanced Industrial Science and Technology, Japan, and Chuo University, Japan
Email: icits2009@m.aist.go.jp
Program Chair: **Kaoru Kurosawa**
Ibaraki University, Japan, Email: icits2009@mx.ibaraki.ac.jp
Local Organizer: **Yukiko Ito**
National Institute of Advanced Industrial Science and Technology, Japan, Email: icits2009@m.aist.go.jp
Advisor: **Hideki Imai**
National Institute of Advanced Industrial Science and Technology, Japan, and Chuo University, Japan
Email: icits2009@m.aist.go.jp

ICITS 2009 Program Committee
- Carlo Blundo(University of Salerno, Italy)
- Paolo D'Arco(University of Salerno, Italy)
- Stefan Dziembowski(UniversitÆ La Sapienza, Italy)
- Serge Fehr(CWI, The Netherlands)
- Juan Garay(AT&T Labs-Research, USA)
- Goichiro Hanaoka(NIAIST, Japan)
- Kaoru Kurosawa,**Chair**(Ibaraki University, Japan)
- Hoi-Kwong Lo(University of Toronto, Canada)
- Keith Martin(Royal Holloway, University of London, UK)
- Ueli Maurer(ETH, Switzerland)
- Jesper Buus Nielsen(University of Aarhus)
- Renato Renner(ETH, Switzerland)
- Rei Safavi-Naini(University of Calgary, Canada)
- Thomas Shrimpton(University of Lugano, Switzerland)
- Doug Stinson(University of Waterloo, Canada)
- Stefan Wolf(ETH, Switzerland)
- Moti Yung(RSA & Columbia University, USA)
- Yuliang Zheng(University of North Carolina, USA)

ICITS 2009 Steering Committee
- Carlo Blundo(University of Salerno, Italy)
- Gilles Brassard(University of Montreal, Canada)
- Ronald Cramer(CWI, The Netherlands)
- Yvo Desmedt,**Chair**(University College London, UK)
- Hideki Imai(NIAIST, Japan)
- Kaoru Kurosawa(Ibaraki University, Japan)
- Ueli Maurer(ETH, Switzerland)
- C. Pandu Rangan(IIT, Chennai, India)
- Rei Safavi-Naini(University of Calgary, Canada)
- Doug Stinson(University of Waterloo, Canada)
- Moti Yung(RSA & Columbia University, USA)
- Yuliang Zheng(University of North Carolina, USA)

ISSN 1813-2065

FIMH 2009

Nice, France : June 3-5, 2009

Functional Imaging and Modeling of the Heart

FIMH 2009 is the Fifth International Conference on Functional Imaging and Modeling of the Heart. This biennial scientific event aims to integrate the research and development efforts in the field of cardiovascular modeling and image analysis.

The main goal is to encourage collaboration between scientists in signal and image processing, imaging, applied mathematics, biophysics, biomedical engineering and computer science, and experts in cardiology, radiology, biology and physiology.

FIMH has established itself as a leading international conference on the methodological aspects of Functional Imaging and Modeling of the Heart, and the peer-reviewed accepted articles are published in the prestigious Lecture Notes in Computer Science proceedings.

Paper Submission → November 28, 2008

All details on our website http://www-sop.inria.fr/asclepios/events/FIMH09/

Conference Chair : **Nicholas Ayache,** *INRIA Sophia-Antipolis*

Program Chair : **Hervé Delingette,** *INRIA Sophia-Antipolis*

Program Committee

E. Angelini, *ENST Paris*
S. Arridge, *University College London*
T. Arts, *Maastricht University*
L. Axel, *NYU Langone Medical Center*
P. Bovendeerd, *Eindhoven University*
D. Chapelle, *INRIA Rocquencourt*
P. Clarysse, *CREATIS-LRMN, University of Lyon*
P. Colli Franzone, *Pavia University*
D. Comaniciu, *Siemens, Princeton*
O. Dössel, *Karlsruhe University*
J. Duncan, *Yale University*
R. Fenici, *Roma Catholic University*
A. Frangi, *Pompeu Fabra University*
M. Garreau, *INSERM, Rennes University*
J.-F. Gerbeau, *INRIA Rocquencourt*
A. Holden, *University of Leeds*
R. Howe, *Harvard University*
P. Hunter, *Auckland University*
P. Kohl, *Oxford University*
B. Lelieveldt, *Leiden University*
C. Lorenz, *Philips Research*
I. Magnin, *CREATIS-LRMN, University of Lyon*
S. Makram-Ebeid, *Philips Healthcare Research*
A. McCulloch, *Univ.California San Diego*
R. MacLeod, *University of Utah*
E. McVeigh, *Johns Hopkins University*
D. Metaxas, *Rutgers University*
J. Montagnat, *I3S CNRS*
W. Niessen, *Erasmus Medical Center*
A. Noble, *Oxford University*
N. Paragios, *Ecole Centrale Paris*
T. Peters, *Robarts Research Institute*
A. Raoult, *Paris Descartes University*
J. Reiber, *Leiden University*
K. Rhode, *Kings College London*
D. Rueckert, *Imperial College London*
F. Sachse, *University of Utah*
G. Seemann, *Karlsruhe University*
M. Sermesant, *INRIA Sophia-Antipolis*
P. Shi, *Rochester Inst. of Technology*
N. Smith, *Oxford University*
M. Sorine, *INRIA Rocquencourt*
J. Spaan, *University of Amsterdam*
L. Staib, *Yale University*
R. Vaillant, *General Electric Med. Systems*
A. Van Oosterom, *CHUV Lausanne*
M. Viergever, *Univ. Medical Center Utrecht*
A. Wahle, *Iowa University*
J. Weese, *Philips Research*
G. Wright, *Sunnybrook Health Sciences*
C. Xu, *Siemens, Princeton*
A. Young, *Auckland University*

INRIA

Abdullah M. Al-Dhafiri

Department of Physics and Astronomy, College of Science, King Saud University, Riyadh, SAUDI ARABIA

High-Quality Plasma-Induced Crystallization of Amorphous Silicon Structures

The investigation of polycrystalline silicon made on glass and carbon coated nickel substrates by aluminum-induced crystallization of amorphous silicon (a-Si) is reported. Aluminum was sputtered onto a-Si films deposited in an ultra-high-vacuum plasma-enhanced chemical vapor deposition (PECVD) system to form Al/a-Si substrate structures. These samples were then vacuum annealed for 30min. at temperatures in the range 150-350℃. X-ray diffractometry (XRD) was utilized to determine the crystallization temperature. Annealing at 275℃ resulted in the formation of crystalline Si as observed by XRD. The presence of these hillocks or bumps after annealing at 275℃ and above confirms that the a-Si has been crystallized.

Keywords: PECVD, polycrystalline Si, Amorphous Si, XRD
Received: 20 November 2008, **Revised**: 27 December, **Accepted**: 3 January 2009

1. Introduction

The crystallization of amorphous silicon (a-Si) is increasingly gaining interest for polycrystalline silicon devices such as thin film transistors (TFTs) and thin-film solar cells [1,2]. In relation to solar cell devices, the crystallization of a-Si offers the opportunity for using low temperature, and therefore low-cost substrates which is vitally important for the reduction of the overall costs of solar cells. However, most attention in the field of crystallization has been given to solid phase crystallization (SPC) [3,4] and laser crystallization (LC) [1,5]. But SPC suffers from long annealing times and rather high temperature (~600°C, which is still too high for large-area substrates) while laser crystallization remains an expensive and complex process. Due to these problems, metal-induced crystallization (MIC) has recently been investigated as an alternative crystallization process for thin-film device fabrication [6-9], although the interaction of metal and a-Si has been studied for many years. Aluminum-induced crystallization (AIC) is one of the most techniques because it has the following advantages: simple processing, process temperature below 600°C, standard industrial fabrication technique, short crystallization time, and also due to the fact that Al has a low resistivity and a good adhesion to a-Si [10-13]. Regarding the crystallization temperature, using AIC, Haque et al. [11] reported as low as 150°C for a-Si:H. It has also been shown that AIC of a-Sibelow the eutectic temperature is a solid phase process [14].

The epitaxial growth model (Fig. 1) explains the formation of a μc-Si:H layer by assuming that during the a-Si:H growth cycle the first atomic layers of the deposition grow epitaxially on the underlying μc-Si:H layer. The remaining a-Si:H part of the grown layer is etched back during the hydrogen plasma cycle, leaving a μc-Si:H layer on the substrate. In this model, the initial nucleation can be explained by chemical transport.

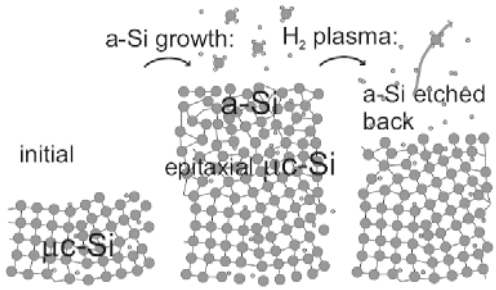

Fig. (1) Schematic representation of the epitaxial growth model: on top of (micro) crystalline silicon (left), a layer is grown during the growth cycle of which the first few atomic layers are epitaxial and the rest is amorphous (middle). During the hydrogen plasma treatment, the amorphous part is preferentially etched away

In the third type, H diffusion plays a dominant role (Fig. 2). Hydrogen diffuses through the material by repeatedly breaking Si–Si and forming intermediate Si–H–Si bonds. Molecular Dynamics simulations show that when the hydrogen atom leaves a strained Si–Si bond, the network relaxes and energy is provided for nucleation. The in-diffusion of hydrogen before the crystallization takes place, is experimentally

 ISSN 1813-2065

observed. A convincing experiment showing that nucleation is due to hydrogen diffusion, is the crystallization of a thick *a*-Si:H layer by repeated hydrogen plasma treatments.

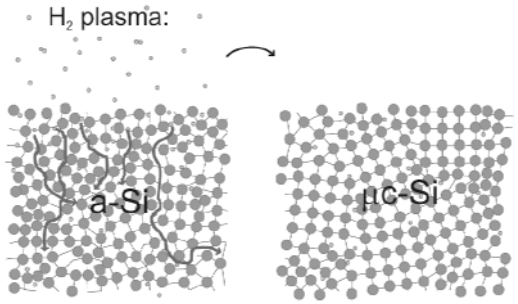

Fig. (2) Schematic representation of the hydrogen diffusion model: during the hydrogen plasma treatment, hydrogen is diffusion in the *a*-Si:H material (left) due to which the crystallinity is enhanced (right)

In this work, AIC of a-Si has been investigated in the form of Al/a-Si substrate structures for a wide range of annealing temperatures. The crystallization process has been investigated by X-ray diffraction (XRD).

2. Experiments

Intrinsic amorphous silicon (a-Si) films of approximately 50nm thick were deposited onto carbon coated nickel substrates using an ultra-high-vacuum plasma enhanced chemical vapor deposition (PECVD) system. After deposition of the a-Si films, the samples were transferred to another chamber where a 50nm thick film of Al was sputter deposited over the a-Si film, using the same system without breaking the vacuum. Corning 7059 glass was used for this purpose. The a-Si and Al thicknesses on the glass substrate were 300nm and 200nm, respectively. In all experiments, the base pressure, sputtering pressure, substrate temperature and RF power density were maintained at $5x10^{-8}$torr, 500mtorr, 240°C and 2W/cm^2, respectively, except the substrate temperature was kept at 40°C during Al sputtering. These nickel and glass substrates were then annealed in vacuum (2mtorr) at 150°C, 200°C, 250°C, 275°C, 290°C, 300°C or 350°C for 30 minutes in a clean optically heated quartz tube furnace. X'pert system using a pw 3710 diffractometer control unit was used for XRD measurements. Cu K_α radiation was provided by a rotating anode x-ray source operating at 45kV and 40mA. X-ray diffraction spectra were taken both under regular θ-2θ and thin- film optics configurations (glancing-angle, parallel-beam geometry). Under the thin-film optics configuration, a 2θ-only scan was performed at a very small fixed θ value of 2.5°. A Xenon-filled proportional counter detector was used for data collection in both configurations.

3. Results and Discussion

Figures (3-8) show XRD spectra of samples annealed at various temperatures for 30 minutes. No crystallization was observed for annealing temperatures of 150°C, 200°C, and 250°C. At 275°C annealing temperature, a small peak appears at a 2θ of 28.5° corresponding to (111) planes, indicating the start of the crystallization of the amorphous silicon.

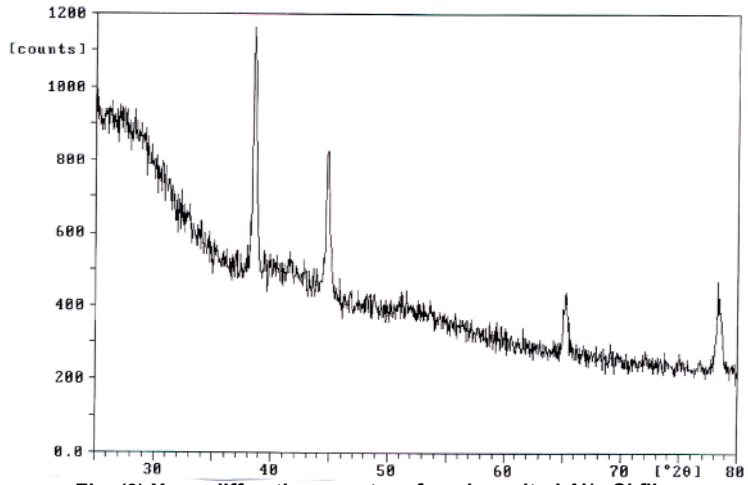

Fig. (3) X-ray diffraction spectra of as-deposited Al/a-Si film

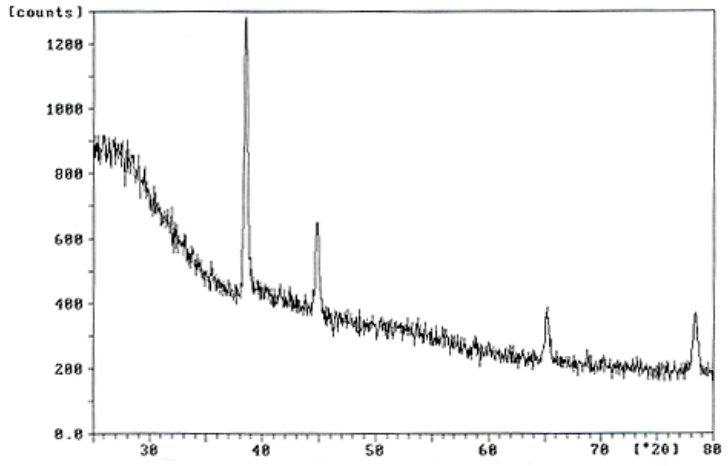

Fig. (4) X-ray diffraction spectra of the Al/a-Si film annealed at 250°C for 30 minutes

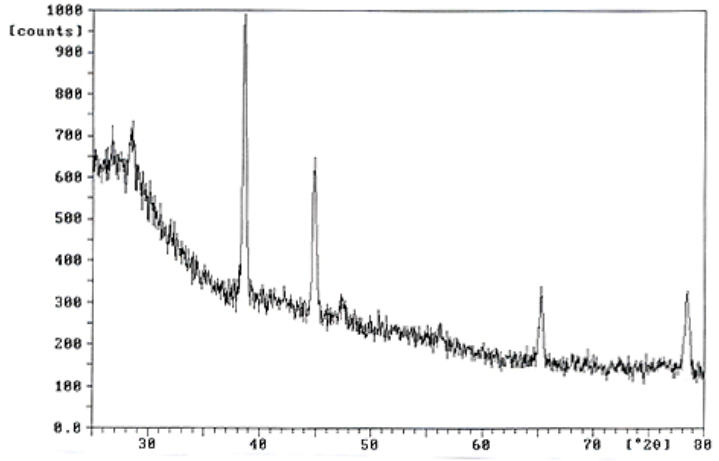

Fig. (5) X-ray diffraction spectra of the Al/a-Si film annealed at 275°C for 30 minutes

Complete crystallization was achieved at temperatures above 300°C, with crystalline Si peaks appearing at 2θ values of 28.5°, 47.3°, 56.1° and 69.2° corresponding to the (111), (220), (311), and (400) planes, respectively, as shown in figures (6), (7) and (8). The polycrystalline Al peaks are also shown in the figure at 2θ values of 38.5°, 44.8°, 65.1° and 78.2°, which are from the (111), (200), (220), and (311) planes, respectively. Similar results have been reported for the configuration where a sputtered a-Si film was deposited onto evaporated Al. In that case crystallization was also observed to occur at temperatures above 300°C [17].

It has also been reported that the crystallization temperature will be slightly higher (310°C) when the configuration takes the form a-Si/Al substrate [15]. It has previously been reported that aluminum assisted crystallization of sputtered a-Si films does not start until the sample is annealed at 300°C for 30 minutes, when the Al is evaporated onto the amorphous silicon films (Al/a-Si) and full crystallization is achieved at 400°C [12]. However, for the case where hydrogenated amorphous silicon was plasma-deposited on evaporated Al (a-Si:H/Al), crystallization required at higher annealing temperatures compared to the other configuration (Al/a-Si:H) [16]. The evaporated Al is exposed to room ambient during its transfer from the evaporator to the cluster tool where either sputtered or plasma deposited amorphous silicon is fabricated.

It seems, therefore, that the native aluminum oxide, which acts as a barrier for crystallization in the plasma deposited sample, is removed during the early phase of sputter deposition of a-Si film. This possibly explains why the crystallization of the sputtered a-Si/sputtered Al and sputtered a-Si/ evaporated Al samples commences at similar temperatures of 300°C when observed by XRD.

ISSN 1813-2065

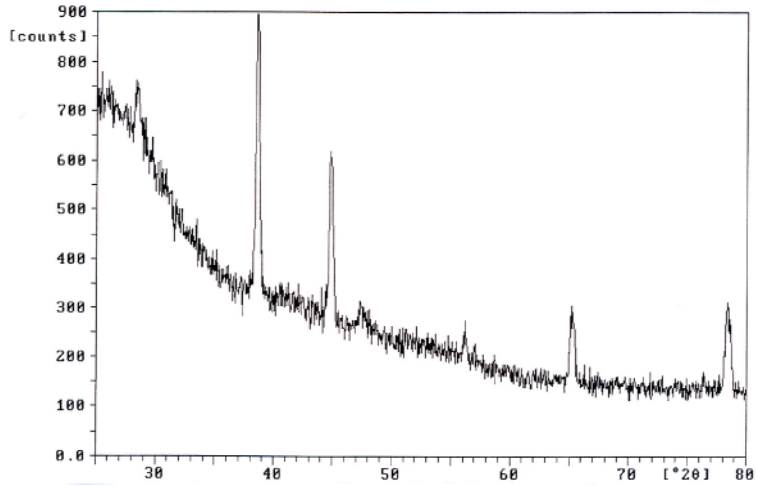

Fig. (6) X-ray diffraction spectra of the Al/a-Si film annealed at 290°C for 30 minutes

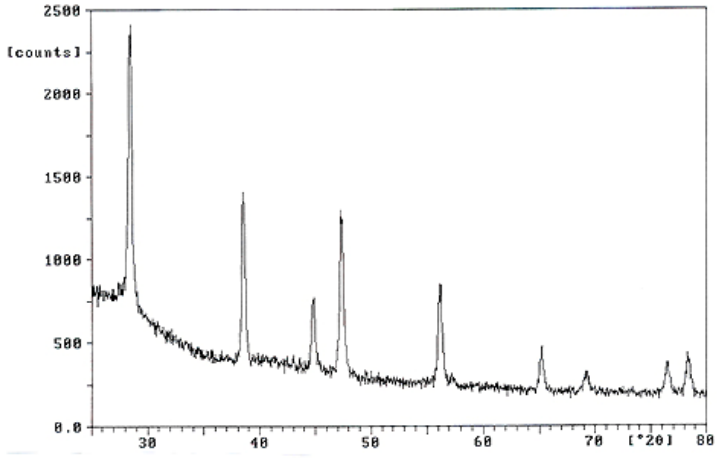

Fig. (7) X-ray diffraction spectra of the Al/a-Si film annealed at 300°C for 30 minutes

It may be noted here that although the glancing-angle XRD patterns show no significant crystallization for samples annealed below 275°C, their EDP show significant levels of crystallization at temperatures above 200°C. This may be due to several reasons. The sensitivity of XRD may be much smaller than TEM/EDP. The electron beam may focus on the crystallized area where the nucleation starts. Or, the initial crystal growth may have some level of preferential orientation, which could not be detected by the thin-film optics using glancing-angle diffraction.

For the case of evaporated Al on plasma-deposited hydrogenated a-Si films (Al/a-Si:H), however, the crystallization was reported to start at temperatures just above 150°C. Hydrogen may be playing a significant role in lowering the crystallization temperature in Al-induced crystallization [7]. Generally, there are a few models for the AIC crystallization process. Haque et al [13] reported that a metal-rich Al-Si mixed phase Al_xSi is formed at the interface at early stage of annealing. Silicon atoms diffuse into the aluminum and aluminum atoms diffuse into the silicon through this defect-rich metastable material. Eventually, atoms which diffuse through the aluminum grain boundaries begin to precipitate on top of the aluminum pad.

Nast and Wenham [17] showed that the Si nuclei formed at Al grain boundaries and that the growth proceeded within the aluminum layer until adjacent Si grains impinged. The overall crystallization process results in the exchange of the layer positions and the formation of a continuous poly-silicon film.

4. Conclusion

Al-induced crystallization of a-Si on two different substrates, glass and carbon coated nickel is investigated in this paper. The interaction between the Al and the a-Si layers is studied in the temperature range 150-350°C. Annealing at 275°C resulted in the formation of crystalline Si as observed by XRD. A new ring appeared in the EDP after annealing Al/a-Si at 350°C or higher. The XRD results confirm that a 30min. annealing at 275°C crystallizes the a-Si.

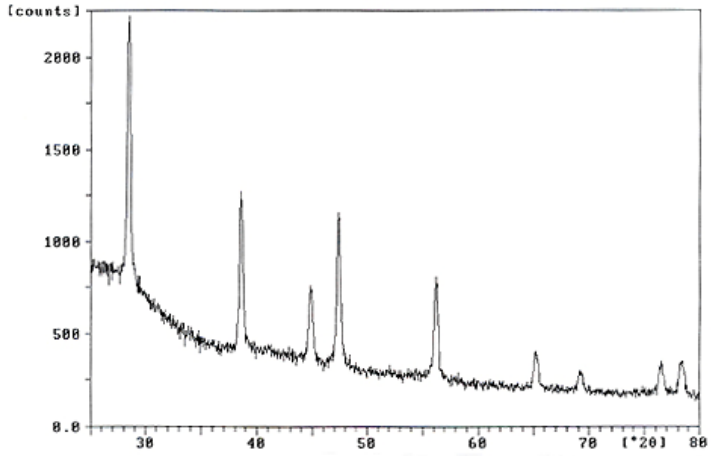

Fig. (8) X-ray diffraction spectra of the Al/a-Si film annealed at 350°C for 30 minutes

References

[1] R.S. Sposili and J.S. Im, *Appl. Phys. Lett*., 69 (1996) 2864-2868.
[2] C. Spinella, S. Lombardo and F. Priolo, *J. Appl. Phys*., 84 (1998) 5383-5414.
[3] R.B. Bergmann et al., *Sol. Energy Mater. and Solar Cells*, 46 (1997) 147-155.
[4] T. Matsuyama et al., *J. Non-Cryst. Solids,* 198 (1996) 940.
[5] K. Ishikawa et al., *Jpn. J. Appl. Phys*., Part 1, 37 (1998) 731-736.
[6] O. Nast et al., *IEEE Trans. Electron Devices,* 46 (1999) 2062-2068.
[7] S.W. Lee and S. Joo, *IEEE Electron Device Lett*., 17(1996) 160-162.
[8] L. Hultman et al., *J. Appl. Phys*., 62 (1987) 3647-3655.
[9] B. Bian et al., *J. Appl. Phys*., 73 (1993) 7402-7406.
[10] A.M. Al-Dhafiri et al., "Structural, Optical, and Electrical Properties of Crystallized Amorphous Silicon Produced by PECVD", *Proc. of 17th European Photovoltaic Solar Energy Conf.,* 22-26, Oct. 2001 (Munich, Germany).
[11] M.S. Haque, H.A. Naseem and W.D. Brown, *J. Appl. Phys.,* 79 (1996) 7529-7536.
[12] A.M. Al-Dhafiri et al., "TEM, SEM, and XRD Studies of Metal Induced Crystallization (MIC) of α-Si", *Sharjah Solar Energy Conf*., 19-22, Feb., 2001 (UAE).
[13] M.S. Haque, H.A. Naseem and W.D. Brown, *J. Appl. Phys.,* 75 (1994) 3928-3935.
[14] T.J. Konno and R. Sinclair, *Philos. Mag., B*66 (1992) 749-765.
[15] A.M. Al-Dhafiri, *J. of Saudi Chemical Society,* 6 (2002) 365-376.
[16] R. Kishore et al., *Electrochem. and Solid State Lett.,* 4 (2001) G14-G16.
[17] O. Nast and S.R. Wenham, *J. Appl. Phys*., 88 (2000) 124-132.

ISSN 1813-2065

IEEE

Call for Papers

Announcing an Issue of the IEEE *JOURNAL OF SELECTED TOPICS IN QUANTUM ELECTRONICS* on Biophotonics

Submission Deadline: July 1, 2009

The Biophotonics field is an emerging biomedical technology that has opened up new horizons for extensive transfer of applicable state-of-the-art techniques coming from the area of quantum electronics, lasers and electro-optics to the life sciences and medicine. Recently, minimally invasive, cost-effective and rapid biophotonics techniques have been developed as potential alternatives to conventional medical methods for diagnostics, monitoring and treatment of a variety of diseases. ***IEEE Journal of Selected Topics in Quantum Electronics*** invites manuscript submissions in the area of biophotonics. The purpose of this issue of JSTQE is to highlight the recent progress and trends in developing of novel biophotonics technologies. Broad technical areas include (but are not limited to):

- **Advanced biophotonics diagnostic methods and systems**
  - Ultrahigh-resolution biophotonics imaging including cellular/intracellular, molecular, 3D endoscopic, photoacoustic, photothermal, diffuse, improved OCT, confocal and multi-photon *in-vivo* bioimaging
  - Spectroscopy-based diagnostics including fluorescence, Raman, elastic scattering, evanescence-wave, near-/mid-IR spectroscopy
  - Novel biophotonics sensing techniques
  - Multi-modal biophotonics diagnostics
- **Progress in minimally-invasive biophotonics therapeutic techniques**
  - Photodynamic cancer therapy
  - Ultrashort pulse laser tissue treatment
  - Precise laser tissue manipulation/ablation in ophthalmology, dentistry, dermatology, cardiology and neurosurgery
  - Novel low-level laser therapeutic techniques and light-tissue-interaction mechanisms at cellular/intracellular level
  - Light-assisted neuron stimulation/growth and cellular/tissue repair
- **Novel approaches in nanobiophotonics**
  - Breaking the diffraction barrier in biophotonics nanoimaging
  - Cellular/intracellular nanobiosensors
  - Nanoparticle-enhanced biophotonics diagnostics/therapeutics
  - Novel nanobiomaterials engineered for nanobiphotonics applications
  - Biocompatibility and phototoxicity of novel nanobiomaterials
- **Development of novel laser, fiber-optic and electro-optic biophotonics tools and devices**

The Guest Editors for this issue are **Ilko Ilev**, U.S. Food and Drug Administration, USA; **Lihong Wang**, Washington University in St. Louis, USA; **Stephen Boppart**, University of Illinois, USA; **Stefan Andersson-Engels**, Lund University Medical Laser Centre, Sweden; and **Beop-Min Kim**, Yonsei University, Korea.

The deadline for submission of manuscripts is **July 1, 2009**; publication is scheduled for May/June **of 2010**.

Online Submission is Mandatory at: http://mc.manuscriptcentral.com/leos-ieee Please select the Journal of Selected Topics Of Quantum Electronics Journal from the drop down menu. Contributed papers should be up to eight pages in length, and invited up to 12 pages. Beyond that, a charge of $220 per page apply. All submissions will be reviewed in accordance with the normal procedures of the Journal.

For inquiries for this Special Issue, please contact:
***JSTQE* Editorial Office - Chin Tan-yan**
IEEE/LEOS, 445 Hoes Lane, Piscataway, NJ 08854, U.S.A.
Phone: 732-465-5813, Email: c.tan-yan@ieee.org

The following supporting documents are required during manuscript submission:

1).doc manuscript (double columned, 12 pages for an Invited Paper, 8 pages for a Contributed paper). Bios of ALL authors are mandatory, photos are optional. You may find the Tools for Authors link useful: http://www.ieee.org/web/publications/authors/transjnl/index.html

2) Completed the IEEE Copyright Form. Copy and paste the link below:
http://www.ieee.org/web/publications/rights/copyrightmain.html

3) Completed Color Agreement/decline form. Please email c.tan-yan@ieee.org to request for this form.

4) .doc list of ALL Authors FULL Contact information as stated below:
Last name (Family name): /First name: Suffix (Dr/Prof./Ms./Mr):/Affiliation:/ Dept: / Address:/ Telephone:/ Fax:/ Email:/ Alternative Email:

Ali H.M. El-Shekh
Eman A.F. Ali
Salah F.A. Ali
Fatma M.M. Aasy

Characteristics of a-Si:H Solar Cell Under Extended Illumination Condition Using NIR Laser

Materials Science Department
Institute of Graduate Studies and Research
Alexandria University,
Alexandria, EGYPT

In this work, characteristics of a-Si:H solar cell under extended illumination condition, using an NIR laser diode, were studied. These characteristics were introduced by calculations of recombination rate, open-circuit voltage and defect growth rate as functions of illumination time. Stabilized open-circuit voltage of 0.04V and photogeneration rate of ~2x10^{21}cm^{-3} were observed. We present measurements on the decline of the open-circuit voltage V_{OC} in a-Si:H solar cells during extended illumination (light-soaking). We used a near-infrared laser that was nearly uniformly absorbed in the intrinsic layer of the cell. At the highest photogeneration rate (about 2x10^{21}cm^{-3}), a noticeable decline (0.01V) occurred within about 10 minutes; V_{OC} stabilized at 0.04V below its initial value after about 200 hours. We found that both the kinetics and the magnitudes of V_{OC} are reasonably consistent with the predictions of a calculation combining a bandtail+defect picture for recombination and a hydrogen-collision model for defect generation.

Keywords: Light soaking, a-Si:H junction, Solar cells, Bandtail effect
Received: 9 December 2008, **Revised**: 2 January 2009, **Accepted**: 9 January 2009

1. Introduction

The metastable degradation of the optoelectronic properties of a-Si:H has been actively studied for more than 25 years. Important progress has been made by many researchers, but a fully satisfactory picture for the effect has never emerged. The difficulty of the metastability problem may, at least in part, be ascribed to the fact that there are probably two difficult, linked problems that must be understood simultaneously. First, it is likely that photocarrier recombination drives metastability, but - even in a single state of an a-Si:H sample - no consensus viewpoint on these recombination processes has emerged. Second, even if one accepts the role of recombination in mediating metastability, there is no consensus viewpoint about how recombination leads to metastable defect generation (or other metastabilities).

The present paper exploits the close connection between the open-circuit voltage V_{OC} measured in an nip solar cell and photocarrier recombination in the bulk, intrinsic-layer material. In particular we report a series of measurements of the time-dependence of V_{OC} in United Solar cells under near-solar illumination. In recent work [1] we reported the temperature-dependence of V_{OC} at solar illumination intensities. We concluded from these studies that, for their as-deposited state, the recombination traffic in our samples flowed predominantly through the valence bandtail states. For the stabilized, light-soaked state recombination traffic appears to be split fairly evenly between the valence bandtail and defects. We emphasize that these conclusions apply to our materials, under near-solar illumination, and near room-temperature; these are, of course, the conditions of greatest practical significance for solar cells.

Using this recombination model as the starting point, we report here that we are able to account for the time-dependent decay of V_{OC} using a straightforward extension of the hydrogen-collision model [2] for defect generation; the extension assumes that mobile hydrogen is generated by bandtail recombination. For our materials, we can also exclude the best known alternative model [3].

There is at least one implications of this perspective on metastability that deserves further investigation. It appears that there is a coincidence of the time-scales at which crossover between bandtail and defect recombination occurs, and at which a stabilized state of the sample is achieved. The coincidence suggests that defect recombination may mediate light-induced annealing.

2. Measurements

For these experiments, six depositions of nip solar cells on stainless steel substrates were done at United Solar Ovonic Corp.. The n and p layers were the same in all depositions; the deposition time for the intrinsic layer was chosen to give

intrinsic layer thicknesses from 185nm to 893nm. The cells were not optimized for solar conversion efficiency, but the individual layers are comparable to those used in high-efficiency cells. Details of the deposition procedures have been given elsewhere [4]. As-deposited properties of the cells were measured under a solar simulator. This paper emphasizes results for the thickest cells, for which the white-light V_{OC} averaged 0.98V and the white-light fill factors averaged 0.66.

Further studies were done using a 30mW, 685nm wavelength near-infrared laser. We chose to use this laser because its wavelength is absorbed fairly uniformly throughout the intrinsic layer of the cells, which substantially simplifies modeling of the measurements. We were able to achieve photocurrent densities in the cells that were comparable to solar illumination.

Measurements of the decline of the open-circuit voltage V_{OC} are presented in Fig. (1). The different symbols indicate measurements for four different laser intensities. We used four different cells on the same substrate for these measurements; the cells had very similar initial properties under white-light. The average photogeneration rates G for each experiment are indicated in the figure; these were calculated from the measured photocurrent density J_p at $V_r = -2V$ using the expression $G=J_p(-V_r)/ed$, where e is the electronic charge and d is the thickness of the intrinsic layer. The measurements for the highest intensity are most comparable to solar illumination (saturated photocurrent density was $18mA/cm^2$ with the laser, and about $15mA/cm^2$ with the solar simulator). The sample temperature was maintained at 294.5K to within better than 0.1K.

An interesting feature of the measurements is that the onset of degradation occurs for later times at lower photogeneration rates. If we define an "onset time" when V_{OC} has declined by 0.01V, it is evident in Fig. 1 that this onset time increases by more than 1000 over the range of photogeneration rates in the figure. For the largest photogeneration rate it appears that V_{OC} is approaching a saturation value within this time window; saturation at longer times is fairly well-established in earlier work on solar cell parameters, defect density, and other optoelectronic properties of a-Si:H.

3. A Modified H-Collision Model

In another paper [1] we presented temperature-dependent measurements on the open-circuit voltage for a-Si:H in its light-soaked and as-deposited states. These measurements are consistent with the model that, for the as-deposited states of a-Si:H, the photocarrier recombination traffic is predominantly through the valence bandtail (through the process of electron capture by a bandtail-trapped hole). Light-soaking then has a surprisingly modest effect: the defect-density rises until recombination traffic is fairly evenly split between the bandtails and the defects.

One important fact that has been established in several light-soaking experiments [3,5-6] is that the defect increases as about the 1/3 power of the light-soaking time: $N_d \propto t^{1/3}$ essentially from the onset of illumination until a saturated state is achieved. The original "SJT" explanation [3] for the $t^{1/3}$ form assumed that recombination traffic through the bandtails R_t generated defects:

$$\frac{dN_d}{dt} \propto R_t \qquad (1)$$

The $t^{1/3}$ form then emerged from a particular recombination model based on the assumption that most recombination traffic went through defects. The particular model that was proposed had the property that the fraction of the recombination traffic through the tails obeyed:

$$\frac{R_t}{G} \propto \frac{1}{N_d^2} \qquad \text{(SJT recombination)} \qquad (2)$$

where G is the carrier photogeneration rate and N_d is the density of defects. With this assumption, one obtains the form usually found by experiment:

$$N_d(t,G) = 3C_{SW}G^{2/3}t^{1/3} \qquad (3)$$

The assumed recombination model appears to be inconsistent with the $V_{OC}(T)$ measurements, in particular in its assumption that the defect recombination traffic R_d is predominant (i.e. that $R_d \approx G$), and thus is unlikely to be the correct explanation for the empirical form (2). The principal alternative to this model is the "hydrogen-collision" model [2], which assumes the existence of a mobile hydrogen density H_m obeying:

$$H_m \propto \frac{G_H}{N_d} \qquad (4)$$

where G_H is the rate at which light generates mobile hydrogen. A mobile hydrogen is assumed to recombine by attaching itself to the density of dangling bond defects N_d. The rate at which new defects are generated obeys the "hydrogen-collision" proportionality:

$$\frac{dN_d}{dt} \propto H_m^2 \qquad \text{(hydrogen-collision)} \qquad (5)$$

The empirical "$t^{1/3}$" form (2) obtains if we assume that $G_H \propto G$.

An interesting alternative to the assumption $G_H \propto G$ is $G_H \propto R_t$. It has often been noted that the large energies dissipated by bandtail recombination of photocarriers make it attractive as an originating event for defect metastability; the energy dissipated is nearly equal to the bandgap E_g, and is certainly larger than

dissipation from recombination through defect levels lying near the center of the gap. One might envision that tail-state recombination might occasionally lead to a peculiar "hydrogen-Auger" process that liberates hydrogen from a nearby, saturated dangling bond. However, the $G_H \propto R_t$ model looks undesirable if one assumes that the SJT recombination model $R_t/G \propto 1/N_d$ is valid. It leads to the behavior $N_d \propto t^{1/5}$, and is thus largely excluded by experiment.

Our measurements of the temperature-dependence of the open-circuit voltage experiments have led us to suggest that R_t/G is of order unity through most of the light-soaking process, which suggests that we reconsider the following, alternative version of the hydrogen-collision equations:

$$\frac{dN_d}{dt} \propto H_m^2 \propto \left(\frac{G_H}{N_d}\right)^2 \propto \left(\frac{R_t}{N_d}\right)^2 \qquad (6)$$

or, collecting several proportionality constants together as C_{SW}:

$$\frac{dN_d}{dt} = C_{SW}\left(\frac{R_t(N_d)}{N_d}\right)^2 \text{ (modified H-collision)} \quad (7)$$

We have indicated that R_t depends upon the defect density; of course, for R_t=G the usual behavior of Eq. (3) obtains.

4. Bandtail+Defect Calculations

In another paper we present the parameters and procedures of a "bandtail+defect" calculation of the open-circuit voltage; the calculation used the AMPS-1D computer program (©Pennsylvania State University).

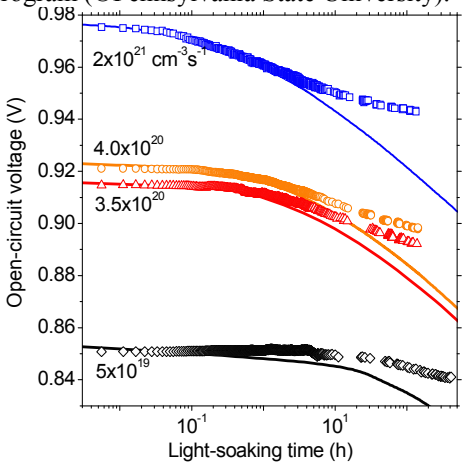

Fig. (1) Decay of the open-circuit voltage with time at four different intensities. The symbols denote the experimental measurements in four cells (893nm i-layer thickness, laser wavelength 685nm) on the same substrate. The lines represent calculations for the "extended hydrogen-collision model" described in the text

In Fig. (1), we have presented (as the four lines) the corresponding calculations for $V_{OC}(t)$ based on Eq. (7), and using the value $C_{SW} = 10^1 cm^{-3}s$ that is typical of direct studies of the defect generation during light-soaking [5,6].

We first used the bandtail+defect calculation to obtain the dependence of the bandtail recombination rate R_t upon the defect density N_d; we assumed a spatially uniform density N_d. The results are illustrated in Fig. (2) (lower panel). We then used this function $R_t(N_d)$ to numerically integrate Eq. (7) to obtain $N_d(t)$; note that Eq. (7) implies that defect generation depends upon the square of R_t. The bandtail+defect calculation also yields V_{OC} as a function of N_d (upper panel of Fig. 2), from which we finally obtained $V_{OC}(t)$.

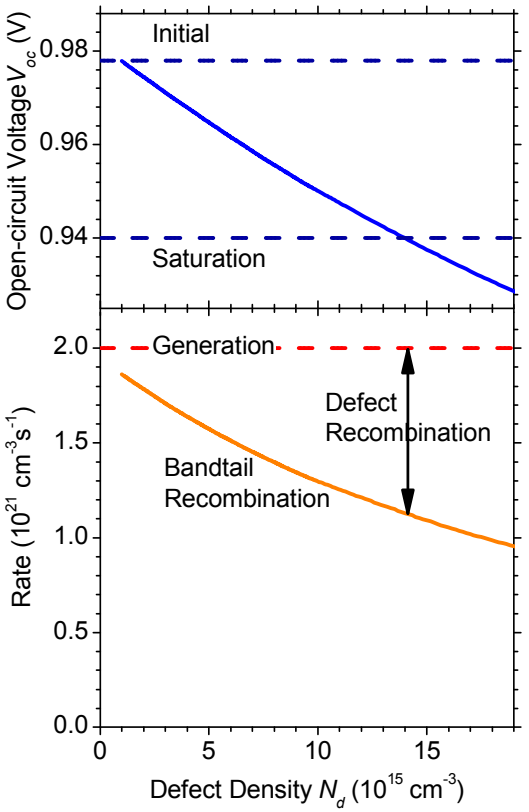

Fig. (2) Bandtail recombination rate R_t and open-circuit voltage V_{OC} calculated as a function of defect density N_d using the bandtail+defect code. The photogeneration rate and defect recombination rate are also shown. The initial experimental value of V_{OC} corresponds to N_d=1x10^{15}cm^{-3}, and we have suggested a saturation value. Note that bandtail recombination is comparable to G throughout this range of defect densities

Experimentally, V_{OC} only declines about 0.04V (to the value denoted "measured saturation"). Fig. (2) indicates that this decline corresponds to a fairly small difference between R_T and G. For the four intensities, the agreement between the experimental measurements and the calculations is fairly good through the initial stages of the decay of V_{OC}. For longer times the measured values for V_{OC} fall much more slowly than predicted by Eq. (7), which undoubtedly corresponds to the onset of the "light-induced"

annealing effects reported previously for defect-density measurements [7].

For our experiments, we used laser illumination that was nearly uniformly absorbed; this choice was part of an effort to simplify modeling and to avoid a non-uniform density of defects. Nonetheless, our assumption of a spatially uniform value for N_d as it grew under light-soaking was not self-consistent with the spatial profiles of R_t that were calculated. For the larger values of the density N_d, the bandtail recombination traffic was reduced in a zone about 100-200nm from the p/i interface compared to values in the middle of the cell. We used R_t values from the middle to do the numerical integration of Eq. (6). For full self-consistency we would have needed to allow for a profile of N_d. The profile would have a reduced density of defects as the p/i interface was approached from the middle. A rough analysis indicates that inclusion of this effect would improve the agreement between the calculations and the measurements slightly, but we have not pursued non-uniform distributions for N_d further.

5. Results and Discussion

As noted earlier, the modified H-collision model, in conjunction with the bandtail+defect recombination model, predicts some deviations from the $t^{1/3}$ form for the dependence of the defect density upon the light-soaking time. We did not do simultaneous measurements of the defect density during light-soaking of the present solar cells. In Fig. (3), we show the predictions of the defect density from numerical integration of Eq. (7) that corresponds to the highest photogeneration rate we used for experiments.

The calculations show the expected $t^{1/3}$ form for the earlier times. There is a softening that occurs around 10 hours, which corresponds well to a change in the recombination mechanism. For lower defect density, the majority of the recombination traffic goes through the bandtail; for larger densities, the majority goes through defects. A $t^{1/5}$ form is a good fit at longer times. Experimentally, after about 10 hours V_{OC} begins to show saturation behavior (cf. Fig. 1), which we attribute to some "light-induced annealing" process. At least for the present samples, it appears that the long-time saturation effect would obscure direct observation of the $t^{1/5}$ regime.

6. Conclusions

It is an interesting coincidence that the crossover time between the two recombination regimes and the time at which light-induced annealing sets in are so similar in the present sample. This apparent coincidence is the reason offered by the present viewpoint for the fact that open-circuit voltages decline only modestly during light soaking (roughly by the thermal voltage k_BT/e=0.025V), as well as for the fact that most direct experiments on the kinetics of the defect density are reasonably consistent with the $t^{1/3}$ form.

It is unlikely that two entirely independent processes would appear on the same timescale. We therefore speculate that the mechanism underlying light-induced annealing is photocarrier recombination through defects.

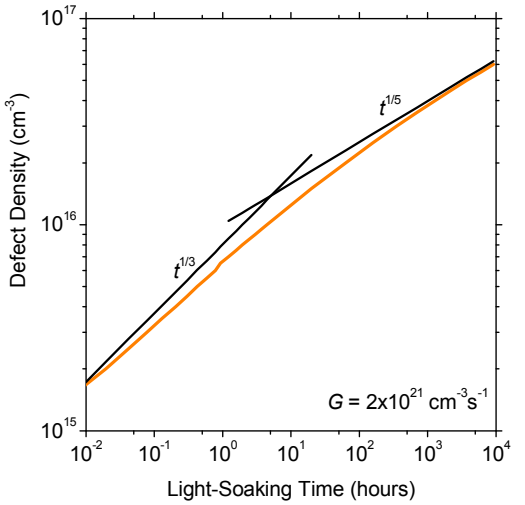

Fig. (3) Calculated growth of the defect density during light-soaking (photogeneration rate $2x10^{21}cm^{-3}s^{-1}$); the calculation was based on the hydrogen-collision model of defect generation (C_{sw}=10cm^{-3}s) and the bandtail+defect recombination model. The calculation shows a cross-over from $t^{1/3}$ to $t^{1/5}$ kinetics when recombination traffic switches from the bandtails to the defects

References

[1] J. Liang et al., in *Amorphous and Nanocrystalline Silicon Science and Technology - 2005*, edited by R. Collins et al., (Materials Research Society Symposium Proceedings Vol. 862 (Pittsburgh, 2005), A13.6.

[2] H.M. Branz, *Phys. Rev., B* l59, 5498 (1999).

[3] M. Stutzmann, W.B. Jackson and C.C. Tsai, *Phys. Rev., B* 32, 23 (1985).

[4] J. Yang, A. Banerjee and S. Guha, *Appl. Phys. Lett.,* 70, 2975 (1997).

[5] H. Park, J. Liu and S. Wagner, *Appl. Phys. Lett.*, 55, 2658 (1989).

[6] T. Unold, J. Hautala and J.D. Cohen, *Phys. Rev., B* 50, 16985 (1994).

[7] H. Gleskova and S. Wagner, *Appl. Phys. Lett.,* (1993).

Call for Papers

6. Optical Networks and Systems

Sponsoring TCs: Optical Networking TC
Communications Switching and Routing TC
Transmission, Access and Optical Systems TC

Chairs: Dominic Schupke, Nokia Siemens Networks (Germany)
Kyriakos Vlachos, University of Patras (Greece)
Jun Zheng, University of Ottawa (Canada)

Research on optical systems has been gathering pace and researchers have been working to produce faster and faster transmission and switching technologies. With rapid advances in optical enabling devices and systems over the past decade, multi-terabit transport networks have now become a reality. In particular, long-haul domains have seen significant induction of advanced dense wavelength-division multiplexing (DWDM) technology. More lately, DWDM and coarse WDM (CWDM) technologies have steadily permeated into the more focused metro/regional and edge domains. A complementary development has also been the rapid maturation of next-generation electronic SONET/SDH grooming technologies. As these paradigm shifts take hold, related standards activities to develop unified provisioning and control-plane architectures for optical and electronic layers have seen much impetus as well. This symposium seeks to showcase the latest developments in key open areas of optical networks and systems, emergent network infrastructures and new optical service paradigms. One of the major themes will be on vertical and horizontal integration. For example, the former entails issues such as Ethernet-optical internetworking, SONET/SDH-WDM multi-granularity grooming, traffic engineering, physical-layer aware networking, as well as the routing, grooming, wavelength assignment and protection/restoration of unicast, multicast or anycast optical connections.

Topics of Particular Interest

- Architectures and technologies for metropolitan, core and local networks
- Optical (WDM/OCDM/OTDM) network and switch architectures
- Optical access networks (PON, EPON, WDM-PON, ...)
- Optical packet, burst and label switching
- Hybrid wireless-optical network architectures
- Routing, wavelength assignment and traffic grooming (multicast, broadcast, anycast, etc.)
- Constraint-based routing
- Horizontal integration: multi-domain optical communications and path computing
- Planning and optimization of optical networks
- Carrier Ethernet
- Next-generation SONET/SDH
- Application-aware optical networking for grid, storage and multimedia services
- Optical and multi-layer network protection and restoration
- Optical virtual private networks
- Control and management for optical networks
- Optical network test beds and field trials
- Optical transmission and system experiments
- System modeling and performance evaluation

ISSN 1813-2065

Rapid Communication

Interfacial Adhesion of PZT Ferroelectric Thin Films Determined by Nano-Indentation Method

X. J. Zheng*
Y. C. Zhou**

**Institute of Fundamental Mechanics and Materials Engineering, Xiangtan University, Xiangtan, Hunan, CHINA*
*** Faculty of Materials and Optoelectronics Physics, Xiangtan University, Xiangtan, CHINA*

We propose an elastic groundsill beam model with piezoelectric effect considered to assess the interfacial adhesion of ferroelectrics thin films, complemented and validated by nano-indentation fracture test on $Pb(Zr_{0.52}Ti_{0.48})O_3$ (PZT) thin films. It was observed from the load-indentation depth curves and atomic force microscopy (AFM) images that the fracture failure of PZT thin films induced by nano-indentations can be divided into three typical stages: no damage, bulging and spallation. The delamination of thin film systems was modeled as an interfacial crack propagation problem, with the energy release rate determined from the elastic groundsill beam model. For PZT thin films deposited on single Si substrate with thickness of 350nm and 450nm, the energy release rates per unit new crack area are in the range of 3.399~52.432J/m^2 and the phase angles are constant of 13.3570.

Keywords: PZT structure, Interfacial adhesion, Thin films, Ferroelectric
Received: 2 February 2009

1. Introduction

$Pb(Zr_xTi_{1-x})O_3$ (PZT) thin film is an important ferroelectric system with potential applications in MEMS, but the conventional models can not be used to analyse the interfacial adhesion and indentation fracture of ferroelectrics thin films accurately because of the piezoelectric effect. The description of fracture toughness of a poled piezoelectric ceramic is very complicated, involving fracture toughness measured perpendicular and parallel to the poling direction [1,2]. In this paper, we propose an elastic groundsill beam model to evaluate the interfacial adhesion of PZT thin films, characterized by energy release rate per unit crack area in nano-indentation test when the largest indentation depth is close to the film thickness. The piezoelectric effects are fully considered in the model. We conducted nano-indentation fracture test on PZT films deposited on single Si substrate by metal organic decomposition (MOD), using a cube corner indenter and atomic force microscopy (AFM). The spallations of the thin film were observed when indentation depths exceeded 13% of the film thickness and when the diamond indenter penetrated through the thin film into the substrate. Interfacial delamination is approximately consisted of the classical mode I and mode II cracks and the corresponding mode II crack dominates the interfacial crack in the ferroelectrics thin films.

2. Theoretical Model

We present a general theory for the axisymmetric indentation of transversely isotropic piezoelectric solids, governed by the following equations

$$\begin{cases} \sigma_{ij} = c_{ijkl}\varepsilon_{kl} - e_{kij}E_k \\ D_i = e_{ikl}\varepsilon_{kl} + \in_{ik} E_k \end{cases} \begin{cases} \sigma_{ij,j} = 0 \\ D_{i,i} = 0 \end{cases} \begin{cases} \varepsilon_{ij} = \dfrac{u_{i,j} + u_{j,i}}{2} \\ E_i = -\phi_i \end{cases}$$

where, σ_{ij}, D_i, ε_{ij}, u_i, E_i and ϕ are stress, electric displacement, strain, displacement, electric field and electric potential, respectively, and c_{ijkl}, ε_{ik} *and* e_{kij} are elastic, dielectric and piezoelectric constants, respectively

The normal indentation of a piezoelectric thin films was considered as shown in Fig. (1a), where h, H, 2α and P_0 are thin film thickness, substrate thickness, apex angle and indentation load, respectively, and $2c$ is the largest imprint made on the surface of the film by the indenter. Combined with the assumption that the indenter is an insulator and does not reach the substrate, we have the relationship between the indentation load P_0 and the largest imprint $2c$ derived by Giannakopoulos and Suresh [3]. Because both the film thickness h and indenter contact region size c are in the nanometer scale, the approximations

$$\frac{\partial u_r}{\partial z} = \frac{\Delta u_r}{h} = \frac{u_r(r,0)}{h}, \frac{\partial u_z}{\partial z} = \frac{\Delta u_z}{c} = \frac{u_z(c,0)}{c},$$
$$Ez = -\frac{\partial \phi}{\partial z} = -\frac{\phi(r,0)}{h}$$

are given. Using the above relationships and boundary conditions, the stress σ_{rr} in the

indentation region of the thin film can be obtained as,

$$\sigma_{rr} = c_{11}\varepsilon_{rr} + c_{12}\varepsilon_{\theta\theta} + c_{13}\varepsilon_{zz} - e_{31}E_z$$

We then present an elastic groundsill beam model as shown in Fig. (1b) to describe the indentation fracture characteristics of thin films, where the indentation depth is assumed to be close to the film thickness. When $\eta=(h/H)\rightarrow 0$.

The constitutive equations of film and substrate are respectively given as

$$\sigma_{rr} = \left(c_{11} - \frac{c_{13}^2}{c_{33}} + \frac{e_{13}^2}{\in_{33}} - \frac{c_{13}e_{13}e_{33}}{c_{33}\in_{33}}\right)\varepsilon_{rr} \quad 0 \le z \le h$$

$$\sigma_{rr} = \frac{8u_2}{k_2+1}\varepsilon_{rr} \quad h \le z \le h+H$$

which is derived from the composite beam theory, with k_2=3-4v_2,v_2 and μ_2.

Being the Poisson ratio and shear modulus of substrate, respectively.

We consider the interface crack problem as shown in Fig. (1c) using the theory of composite beam. The interface intensity factors K_1 and K_2 reduce to the classical mode I and mode II factors K_I and K_{II},

$$K_I = \frac{1}{\sqrt{2}}\left[\frac{P}{\sqrt{h}}\cos\omega + \frac{2\sqrt{3}M}{\sqrt{h^3}}\sin\omega\right]$$

$$K_{II} = \frac{1}{\sqrt{2}}\left[\frac{P}{\sqrt{h}}\sin\omega + \frac{2\sqrt{3}M}{\sqrt{h^3}}\cos\omega\right]$$

where the angle ω is a function related with the Dundurs' parameters α and β [4]. The energy release rate per unit new crack area can be then written in terms of the complex stress intensity factor,

$$G = \frac{c_1 + c_2}{16\cosh^2\pi\varepsilon}|K|^2, K = K_I + iK_{II}, \varepsilon = \frac{1}{2\pi}\ln\frac{1-\beta}{1+\beta}$$

where, ε is the bimaterial constant.

3. Experiment

The indenter was driven perpendicularly into, then out of, PZT thin films prepared by MOD. In order to understand indentation fracture process of PZT, we used three types of peak indentation loads to induce the fracture of the samples and recorded the corresponding load-indentation depth curves. Each indentation experiment consisted of loading, holding, and unloading completely. After the unloading, associated crack patterns were examined by AFM. The typical load-displacement curves and AFM image of indentations made at indentation loads are given as Fig. (2) and Fig. (3).

To determine the parameters for the theoretical model, we obtain elastic, piezoelectric and dielectric constants of PZT thin films from the reference [3]. The interfacial crack length 2a, the largest imprint 2c at the peak indentation load P_0, and the residual depth could be obtained from the AFM image. As a result the interfacial adhesion of PZT thin films could be determined from our theoretical model given as Eq. (5).

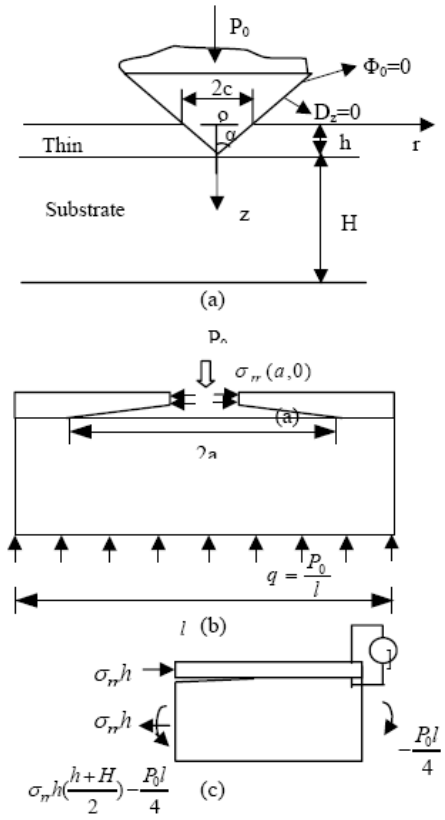

Fig. (1)

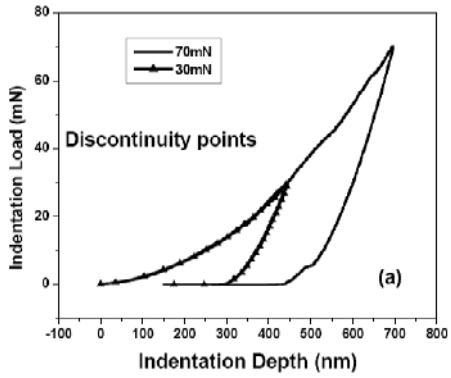

Fig. (2)

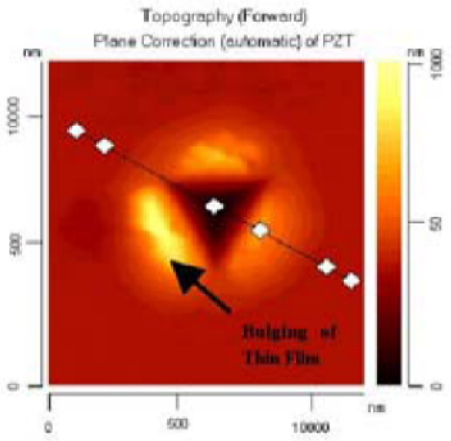

Fig. (3)

ISSN 1813-2065

4. Results and Discussions

From the load-indentation depth curves and AFM images, the different failure process can be observed. Summarizing the experimental observation, one concludes that each discontinuity indicates the point where the nano-indenter was driven from one medium into another, and the propagation of interfacial cracks increases with increasing indentation load.

After determining the radius of the residual indent mark region c, the interface intensity factors K_1, K_2, and energy release per unit new crack area G can be calculated by equations (4) and (5). The energy release rate versus the interfacial fracture area is shown in Fig. (4), which showed that the energy release rate decreased as the interfacial crack length increased.

5. Concluding Remarks

We proposed a model to measure interfacial adhesion in ferroelectric thin films. An elastic groundsill beam model taking into account the piezoelectric effect is developed to describe the interfacial crack for ferroelectrics thin films when the indentation depth is close to the film thickness. The model was validated by nano-indentation tests made on PZT thin films, where the elastic modulus and hardness of PZT thin films were determined from load-indentation depth curves, and energy release rate and stress intensity factors were calculated.

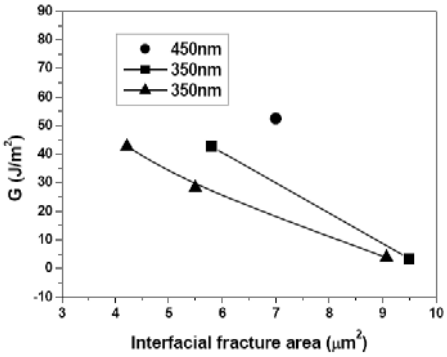

Fig. (4)

References

[1] K. Uchino, **"Piezoelectric Actuators and Ultrasonic Motors"**, Kluwer Academic Press (Boston, 1997).

[2] K. Mehta and A. Virkar, *J. Amer. Ceram. Soc*., 73(3) (1990) 567-574.

[3] A.E. Giannaropoulos and S. Suresh, *Acta Mater.,* 47(7) (1999) 2153-2164.

[4] Z. Suo and J.W. Hutchinson, *Inter. J. Fract*., 43 (1990) 1-18.

THE IRAQI JOURNAL OF APPLIED PHYSICS
EDITORIAL BOARD

COPYRIGHY RELEASE

Iraqi Journal of Applied Physics (IJAP)

We, the undersigned, the author/authors of the article titled
……
……
……
……
……
……
that is presented to the Iraqi Journal of Applied Physics (IJAP) for publication, declare that we have neither taken part or full text from any published work by others, nor presented or published it elsewhere in any other journal. We also declare transferring copyrights and conduct of this article to the Iraqi Journal of Applied Physics (IJAP) after accepting it for publication.

The authors will keep the following rights:

1. **Possession of the article such as patent rights.**
2. **Free of charge use of the article or part of it in any future work by the authors such as books and lecture notes without referring to the IJAP.**
3. **Republishing the article for any personal purposes of the authors after taking journal permission.**

To be signed by all authors:

Signature:……..date: ……..

Printed name: ……

Signature:……..date: ……..

Printed name: ……..

Signature:……..date: ……..

Printed name: ……..

Correspondence address:
……
……
……
Address:……
……
……
Telephone:……..email: ……..

Note: Please complete and sign this form and mail it to the below address with your manuscript

The Iraqi Journal of Applied Physics,
P. O. Box 55259, Baghdad 12001, IRAQ
Website: www.ijap.org, Email: editor@ijap.org, editor_ijap@yahoo.co.uk
Tel.: +964-7901274190

 ISSN 1813-2065 Printed in IRAQ

IRAQI JOURNAL OF APPLIED PHYSICS

CONTENTS